Classification of singular points in the polarization field of the cosmic microwave background and eigenvectors of the Stokes matrix

A. D. Dolgov
Theoretical Astrophysics Center, DK-2100 Copenhagen, Denmark;
Institute of Theoretical and Experimental Physics, 117259 Moscow, Russia

A. G. Doroshkevich
Theoretical Astrophysics Center, DK-2100 Copenhagen, Denmark

D. I. Novikov
Department of Physics and Astronomy, University of Kansas, 66045 Lawrence, Kansas, USA;
Astro-Space Center of Lebedev Physical Institute, Russian Academy of Sciences, 117924 Moscow, Russia

I. D. Novikov
Theoretical Astrophysics Center, DK-2100 Copenhagen, Denmark;
Astro-Space Center of Lebedev Physical Institute, Russian Academy of Sciences, 117924 Moscow, Russia;
University Observatory; NORDITA, DK-2100 Copenhagen, Denmark

(Submitted 11 February 1999)
Pis'ma Zh. Éksp. Teor. Fiz. **69**, No. 6, 395–401 (25 March 1999)

An analysis is made of the singularities of the polarization field of the cosmic microwave background, where the polarization is equal to zero. It is found that the classification of the singular points differs from the usual three types known in ordinary differential equations. The new statistical properties of the polarization field are discussed, and new methods to detect the presence of primordial tensor perturbations are indicated. © *1999 American Institute of Physics.*
[S0021-3640(99)00106-1]

PACS numbers: 98.70.Vc, 98.80.Es

In the coming years the measurements of the angular anisotropies of the intensity of cosmic microwave background (CMB) by the cosmic missions MAP and PLANCK will possibly present one of the most promising methods of studying the early universe as well as of precisely measuring the basic cosmological parameters (see, e.g., Ref. 1 and references therein). In addition to the anisotropies of the intensity, it is possible, though more difficult, to measure the polarization of the radiation. The polarization is a secondary effect induced by the scattering of the anisotropic radiation field on electrons in the cosmic plasma. The corresponding measurements of the CMB polarization are planned to be performed in the coming space missions.

The polarization field is described by a traceless 2×2 matrix which can be decom-

posed into a sum of three Pauli matrices σ_i with coefficients known as the Stokes parameters:[2]

$$\mathbf{a}=\xi_i\sigma_i\,. \tag{1}$$

As is well known circular polarization does not arise in Thomson scattering (because of parity conservation), so that $\xi_2=0$ and the matrix **a** is symmetric. Usually it is parametrized in the form

$$\mathbf{a}=\begin{pmatrix} Q & U \\ U & -Q \end{pmatrix}. \tag{2}$$

The sources of polarization are anisotropies of the radiation field, induced by different types of perturbations, namely scalar, tensor, and vector ones. Vector perturbations decay in the early universe but may arise on small scales at later stages and influence the CMB polarization in the case of reionization.

The geometrical properties of the polarization field can yield important cosmological information.[2–9] The importance of studying singular points of the polarization field, where $Q=U=0$, was emphasized in Ref. 10. In that paper a geometric classification and a statistics of the singular point were proposed. This was done in terms of the fields Q and U which directly enter polarization matrix. The latter are two-dimensional (2D) tensor fields and have the appropriate transformation properties under rotation of the coordinate system.

In this paper we will investigate the classification of singular points of eigenvectors of the polarization matrix **a**. Though the positions and statistics of the singular points remains the same, their types could be quite different. The eigenvalues are easily found:

$$\lambda_{1,2}=\pm\sqrt{Q^2+U^2}, \tag{3}$$

and the eigenvector corresponding to the positive λ is

$$\mathbf{n}^{(1)}\equiv(n_x,n_y)\sim(U,\sqrt{Q^2+U^2}-Q). \tag{4}$$

This vector determines direction of maximum polarization and up to a normalization factor coincides with the direction of the vector **P** considered in Refs. 4, 6, and 7 or orthogonal to it, depending upon the sign of the coefficient functions.

The behavior of the vector field $\mathbf{n}^{(1)}$ in the vicinity of the singular points of the polarization, $Q=U=0$, is determined by the equation

$$\frac{dy}{dx}=\frac{n_y}{n_x}=\frac{\sqrt{Q^2+U^2}-Q}{U}. \tag{5}$$

Analysis of singular points of differential equations when both numerator and denominator can be expanded in Taylor series is well known and can be found, e.g., in Ref. 11. In the usual case the following singular points can exist: focus, saddle, and knot. In our case the situation is more complicated due to the presence of the square root in the numerator which is generically nonanalytic at the points where $Q=U=0$. At this stage a question may arise why it is assumed that Q and U are analytic functions expandable in Taylor series (at least up to first-order terms) around the points where $Q=U=0$, while the component of the eigenvectors are not. The reason for that is the following. The

matrix elements of the polarization matrix Q and U are directly related to the anisotropy of the cosmic microwave radiation through the amplitude of photon–electron scattering. There is no reason to expect these quantities to have a square-root singularity, where their first derivative tends to infinity. On the other hand, the eigenvectors of the matrix **a** mathematically contain the square root $\sqrt{Q^2+U^2}$ and so are singular at $Q=U=0$. The analysis of singularities of the vector field $\mathbf{n}^{(1)}$ can be done as follows. We assume that Q and U are expanded near singular points as

$$Q=a_1x+a_2y, \quad U=b_1x+b_2y. \tag{6}$$

In the case when the matrix

$$\mathbf{M}=\begin{pmatrix} a_1 & a_2 \\ b_1 & b_2 \end{pmatrix} \tag{7}$$

is nondegenerate, $\det \mathbf{M}\neq 0$, it is convenient to introduce the new coordinates:

$$\xi=a_1x+a_2y, \quad \eta=b_1x+b_2y,$$
$$x=A_1\xi+A_2\eta, \quad y=B_1\xi+B_2\eta. \tag{8}$$

Clearly the types of the singular points do not change under this coordinate transformation. It is simpler to do the further analysis in polar coordinates:

$$\xi=\rho\cos\phi, \quad \eta=\rho\sin\phi. \tag{9}$$

Equation (5) in these new polar coordinates can be rewritten as

$$\frac{d(\ln\rho)}{dt}=\frac{2}{t^2+1}\frac{N}{D}, \tag{10}$$

where $t=\tan(\phi/2)$, and

$$N=-A_2t^3+t^2(B_2-2A_1)+t(2B_1+A_2)-B_2, \tag{11}$$

and

$$D=A_1t^3-t^2(B_1+2A_2)+t(2B_2-A_1)+B_1. \tag{12}$$

Barring the degenerate case of $A_1=0$, we may take $A_1=1$ without loss of generality.

The behavior of singular points depends upon the roots of denominator D. Let us first consider the case when it has three real roots, $t_{1,2,3}$. The solution of Eq. (10) in this case can be written as

$$\frac{r}{r_0}=(t^2+1)\prod_j |t-t_j|^{2\nu_j}, \tag{13}$$

where r_0 is an arbitrary constant and the powers ν_j are

$$\nu_1=-\frac{(1+t_1^2)(1+t_2t_3)}{2(t_1-t_2)(t_1-t_3)} \tag{14}$$

and so on by cyclic permutation of indices. Since it can be shown that $\Sigma\nu_j=-1$, the points where $t^2\to\infty$ are not generally singular. It can be easily checked that either all $\nu_j<0$ or any two of them are negative and one is positive. In the first case (see Fig. 1a) the singular point resembles the usual saddle, with the only difference that there are three

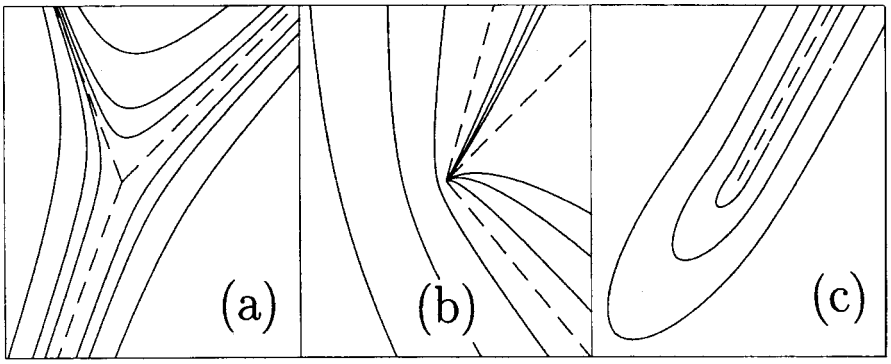

FIG. 1. Integral curves for three different types of singular points: a) saddle, b) beak, and c) comet. The dashed lines show peculiar solutions (separatrices).

linear asymptotes/sep aratrices and not four, as in the usual case. We will call it also a ''saddle.'' If one of the ν_j is positive (say $\nu_1>0$), so that r becomes zero at $t=t_1$, the behavior of the direction field near this point is quite different from the usual case. The field line cannot be continued along $\phi=\phi_1$ into $\phi=\phi_1+\pi$ as can be done in the usual case. We will call this type of singularity a ''beak'' (see Fig. 1b).

In the case of one real root of the denominator D the solution has the same form as (13) but now, e.g., the exponents ν_2 and ν_3 are complex conjugates. The solution can be written as

$$r/r_0=(t^2+1)|t-t_2|^{4\mathrm{Re}\,\nu_2}\exp(4\beta\,\mathrm{Im}\,\nu_2)(t-t_1)^{2\nu_1}, \tag{15}$$

where $\beta=\tan^{-1}[\mathrm{Im}\,t_2/(t-\mathrm{Re}\,t_2)]$. The real root ν_1 is negative, as is seen from Eq. (14) and thus r does not vanish in the vicinity of such a singular point. The polarization direction field for this case is presented in Fig. 1c. This type of singularity can be called a ''comet.''

One can estimate the density of different singular points in the following way (see, e.g., Refs. 4 and 10). All singular points correspond to the case when both $Q=0$ and $U=0$. The number density of these points is proportional to

$$dQdU=\det\begin{pmatrix} Q_x & Q_y \\ U_x & U_y \end{pmatrix} dxdy, \tag{16}$$

and thus the density is given by the average value of the determinant $d=Q_xU_y-Q_yU_x$. It can be easily checked that the saddle-type singularity takes place if $d>0$, which is the same condition as for normal saddles in the field determined by the equation $dy/dx=Q/U$ (see Ref. 10). It can be shown that saddles comprise 50% of all singular points $\langle n_s\rangle=0.5\langle n\rangle$, where n is the number density of all singular points. Calculations of the number of beaks and comets are more complicated and can be found numerically. According our estimates the surface densities for beaks and comets are $\langle n_b\rangle\approx0.052\langle n\rangle$ and $\langle n_c\rangle\approx0.448\langle n\rangle$, respectively. We note that the probability of appearance of saddles, beaks, and comets for a random choice of Q_x, Q_y, U_x,U_y, is $W_s=0.500$, $W_b\approx0.116$, $W_c\approx0.384$, respectively.

As we have said, the polarization of cosmic microwave radiation arises due to anisotropy of the radiation field. It is a linear functional of the field, and in the case of scalar perturbations the only way to construct a two-dimensiona l tensor quantity is to use second derivatives of a scalar function Ψ, as is argued in Refs. 9 and 12, for example. The matrix elements of the traceless symmetric matrix (2) are constructed uniquely as

$$a_{ij}=2\partial_i\partial_j\Psi-\delta_{ij}\partial^2\Psi. \tag{17}$$

For the functions Q and U, this gives

$$Q=(\partial_x^2-\partial_y^2)\Psi, \quad U=2\partial_x\partial_y\Psi. \tag{18}$$

In principle one may use also the invariant two-dimensional antisymmetric (pseudo)tensor ϵ_{ij}, but parity conservation forbids its appearance in the polarization matrix in the case of scalar perturbations. For tensor perturbations there could be specific ''external'' directions in the space, and parity considerations do not preclude using ϵ_{ij} in the matrix (2) (see below). For the specific form (18) of the polarization matrix there exists a particular (pseudo)scalar quantity which vanishes in the absence of gravitational perturbations:[6,7]

$$B=\epsilon_{ij}\partial_k\partial_i M_{kj}. \tag{19}$$

Written explicitly, it reads

$$B=(\partial_x^2-\partial_y^2)U-2\partial_x\partial_y Q. \tag{20}$$

It clearly vanishes for Q and U given by expressions (18).

In the case when tensor perturbations are present, there is more freedom in the polarization matrix **a**; terms proportional to ϵ_{ij} are permitted, and the symmetric matrix **a** may be expressed through second derivatives of two independent scalar functions:

$$M_{ij}=2\partial_i\partial_j\Psi-\delta_{ij}\partial^2\Psi+\epsilon_{ik}\partial_k\partial_j\Phi \;\; \epsilon_{jk}\partial_k\partial_i\Phi. \tag{21}$$

This is a general decomposition of symmetric traceless tensor in two dimensions (see, e.g., Ref. 6).

With the inclusion of tensor perturbations the functions Q and U take the form

$$Q=(\partial_x^2-\partial_y^2)\Psi+2\partial_x\partial_y\Phi,$$

$$U=2\partial_x\partial_y\Psi-(\partial_x^2-\partial_y^2)\Phi. \tag{22}$$

The scalar B is expressed in terms of the fourth derivatives of Φ as

$$B=\partial^4\Phi. \tag{23}$$

The difference between scalar and tensor perturbations appears only in the fourth derivatives of the generating scalar functions Φ and Ψ, while the structure of their singularities is determined by the third derivatives. Thus the types of the singularities are the same for both types of perturbations. There are statements in the literature that in the case of scalar perturbations vector **n** cannot have a curl, while tensor perturbations do produce a curl (see Sec. 4 of Ref. 13).

However, the polarization tensor is not a vector but a second-rank tensor, and direct analogy with a vector field is not applicable. In the general case of singular points considered above the curl is not equal to zero for any type of perturbations. An explicit

example of scalar generating function Ψ being a function only of $r=\sqrt{x^2+y^2}$ near the singularity point shows that the latter may be either center or knot. These points are absent in our list of three presented above due to a specific degeneracy of this example.

Thus to summarize, the singular points of the vector field $\mathbf{n}^{(1)}$, which is the eigenvector of polarization matrix corresponding to the direction of maximum polarization can be generically of the following three types (see above): saddle and beak (with three separatrices), and comet (one separatrix). In degenerate case, when some of the coefficients or their combinations (e.g., determinants) may be zero, then there could be some other types singularities which we have not considered here.

The functions Q and U are usually assumed to be independent Gaussian variables with equal variance (Ref. 4):

$$\langle Q^2\rangle=\langle U^2\rangle=\sigma_0^2. \tag{24}$$

Their first derivatives are also independent and uncorrelated with the functions and have a variance

$$\langle Q_iQ_j\rangle=\langle U_iU_j\rangle=\delta_{ij}\sigma_1^2/2, \tag{25}$$

where $Q_i=\partial Q/\partial x^i$, etc. All other correlators are zero. However, the fact that in the case of scalar perturbations both functions Q and U as well as their derivatives are determined by a single generating scalar function Ψ imposes some conditions on the correlators of the second derivatives. In particular, the variances of the second derivatives Q_{ij} and U_{ij} are unequal, and these fields are correlated. The list of nontrivial correlators is as follows:

$$\begin{aligned}
&\langle Q_{xx}^2\rangle=\langle Q_{yy}^2\rangle=\frac{7}{16}\sigma_2^2, \quad \langle U_{xx}^2\rangle=\langle U_{yy}^2\rangle=\frac{5}{16}\sigma_2^2,\\
&\langle Q_{xx}Q_{yy}\rangle=\langle Q_{xy}Q_{xy}\rangle=\frac{1}{16}\sigma_2^2, \quad \langle U_{xx}U_{yy}\rangle=\langle U_{xy}U_{xy}\rangle=\frac{3}{16}\sigma_2^2,\\
&\langle Q_{xx}U_{xy}\rangle=\langle Q_{xy}U_{xx}\rangle=\frac{1}{16}\sigma_2^2, \quad \langle Q_{yy}U_{xy}\rangle=\langle Q_{xy}U_{yy}\rangle=-\frac{1}{16}\sigma_2^2,\\
&\langle Q_{xx}Q\rangle=\langle Q_{yy}Q\rangle=\langle U_{xx}U\rangle=\langle U_{yy}U\rangle=-\sigma_1^2/2,
\end{aligned} \tag{26}$$

where $\sigma_2^2\equiv\langle(Q_{xx}+Q_{yy})^2\rangle=\langle(U_{xx}+U_{yy})^2\rangle$. Note that the asymmetric correlators in the third line are nonvanishing.

These properties permit one in principle to discriminate and detect the contributions of tensor (or vector) perturbations to the polarization of the CMB by measuring the variance of the second derivatives of the Stokes parameters. In particular, for purely scalar perturbations one should expect

$$\langle Q_{xx}^2\rangle/\langle U_{xx}^2\rangle=\langle Q_{yy}^2\rangle/\langle U_{yy}^2\rangle=7/5, \quad \langle(U_{xx}-U_{yy})^2\rangle=4\langle Q_{xy}^2\rangle. \tag{27}$$

A deviation from this number would indicate a contribution from other, nonscalar types of perturbations. The last equality in (27) corresponds to $B=0$ (see Eq. (20)). The property $B=0$ as a test for the absence of scalar perturbations was pointed out in previous works (see, e.g., Ref. 7).

An interesting quantity which allows one to relate global characteristics of a random field to local properties is the Euler characteristic χ_E (see Ref. 14). As was noted in Ref. 15, this value is closely linked to the critical value of the polarization amplitude, $P=\sqrt{Q^2+U^2}$, at which percolation of the regions of high polarization occurs. According to Ref. 14, percolation begins at the polarization amplitude corresponding to $\chi_E=0$.

This critical amplitude was estimated in Ref. 10 where it was found that percolation takes place for $p=1$, where $p=P/\sigma_0$ is the dimensionless amplitude of polarization at unit variance. We estimated this quantity in somewhat different way than was done in Ref. 10. In the 2D case the required value is defined by an equation

$$\chi_E \propto \langle p_{xx}+p_{yy}\rangle p\exp(-p^2/2)\propto (p^2-1)\exp(-p^2/2) \tag{28}$$

that is identical to result obtained in Ref. 10. Though the statistical distribution we used is different from the one of Ref. 10, we got the same result: percolation occurs at $p=1$. Let us recall that for the 2D Gaussian fields $\chi_E \propto p\exp(-p^2/2)$ and percolation occurs at $p=0$. As follows from (17)–(22) the same results are valid for all three types of the perturbations of polarization field. These topics will be discussed in more detail in a subsequent paper.[16]

This work was supported in part by Danmarks Grundforskningsfond through its funding of the Theoretical Astrophysical Center (TAC), the Danish Natural Science Research Council through Grant #9401635, and in part by NSF-NATO Fellowship (DGE-9710914) and by NSF EPSCOR program. One of us (D. N.) thanks M. Kamionkowski for helpful discussions.

[1] W. Hu, N. Sugiyama, and J. Silk, Nature (London) **386**, 37 (1997).
[2] M. A. Basko and A. G. Polnarev, Sov. Astron. **24**, 3 (1979).
[3] A. G. Polnarev, Sov. Astron. **29**, 607 (1985).
[4] J. R. Bond and G. Efstathiou, Mon. Not. R. Astron. Soc. **226**, 655 (1987).
[5] U. Seljak, Astrophys. J. **482**, 6 (1996).
[6] M. Kamionkowski, A. Kosowsky, and A. Stebbins, Phys. Rev. D **55**, 7368 (1997).
[7] M. Zaldarriaga and U. Seljak, Phys. Rev. D **55**, 1830 (1997).
[8] W. Hu and M. White, New Astron. **2**, 323 (1997).
[9] U. Seljak and M. Zaldarriaga, http://xxx.lanl.gov/abs/astro-ph/9805010.
[10] P. D. Naselsky and D. I. Novikov, http://xxx.lanl.gov/abs/astro-ph/9801285, Astrophys. J. (to be published).
[11] I. N. Bronshtein and K. A. Semendyaev, *Handbook of Mathematics* (in Russian), M.: Gostekhizdat, 1955.
[12] U. Seljak and M. Zaldarriaga, Astrophys. J. **469**, 437 (1996).
[13] M. Kamionkowski, http://xxx.lanl.gov/abs/astro-ph/9803168.
[14] P. Coles, A. Davies, and R. Pearson, Mon. Not. R. Astron. Soc. **281**, 1375 (1996).
[15] K. R. Mecke and H. Wagner, J. Stat. Phys. **64**, 843 (1991).
[16] A. Dolgov, A. Doroshkevich, D. Novikov, and I. Novikov, in preparation.

Published in English in the original Russian journal. Edited by Steve Torstveit.

Possible manifestations of the existence of a fourth-generation neutrino

Yu. A. Golubkov*
Kosmion Science and Education Center for Cosmomicrophysics, 125047 Moscow, Russia; M. V. Lomonosov Moscow State University, 119899 Moscow, Russia

R. V. Konoplich†
Kosmion Science and Education Center for Cosmomicrophysics, 125047 Moscow, Russia; Moscow State Engineering-Physics Institute, 115409 Moscow, Russia

R. Mignani‡
Dipartimento di Fisica ''E. Amaldi'' Universitá di Roma III, 00146 Rome, Italy; INFN, Sezione di Roma III

D. Fargion§
Dipartimento di Fisica Universitá degli Studi ''La Sapienza,'' 00185 Rome, Italy; INFN, Sezione di Roma I

M. Yu. Khlopov**
Kosmion Science and Education Center for Cosmomicrophysics, 125047 Moscow, Russia; Moscow State Engineering-Physics Institute, 115409 Moscow, Russia; M. V. Keldysh Institute of Applied Mathematics, 125047 Moscow, Russia

(Submitted 15 February 1999)
Pis'ma Zh. Éksp. Teor. Fiz. **69**, No. 6, 402–406 (25 March 1999)

A fourth generation of fermions predicted by the phenomenological heterotic string models can possess a new, strictly conserved charge. Among other things, this leads to the hypothesis of the existence of a fourth massive stable neutrino. A comparison of this hypothesis with the data obtained in the DAMA underground experiment to search for massive weakly-interacting cosmic particles with hidden mass and with the EGRET measurements of the >1 GeV galactic gamma-ray background gives a value $m \approx 50$ GeV for the possible mass of the fourth neutrino. It is shown that the hypothesis can be checked in accelerator experiments. The positron signal from annihilation of massive relic neutrinos in the galaxy is calculated. A search for this signal is is within the reach of planned cosmic-ray investigations. © *1999 American Institute of Physics.* [S0021-3640(99)00206-6]

PACS numbers: 14.60.St, 98.70.Rz

Superstring theory[1] has been viewed in the last ten years as a promising approach to the construction of a ''theory of everything,'' making it possible, ideally, to find all basic parameters of the theory from first principles. However, the number of possible realizations of string theory that reproduce the Standard Model in the low-energy limit is extremely large. For this reason, analysis of the phenomenology of superstring theory to

narrow the admissible range of parameters of the hidden sector of the theory is very important. The existence of at least four generations of fermions and the phenomenology of broken E_6 symmetry, including the symmetry of the Standard Model, together with $N=1$, supergravity, and the (broken) E_8' symmetry of shadow particles and their interactions, are important consequences of superstring theory[2] that cicumscribe the admissible manifestations of the hidden sector of the simplest variants of the heterotic-string model. Identifying the fourth generation of fermions with states possessing a new, strictly conserved charge that is not characteristic of the three known generations, we arrive at, specifically, the fact that the lightest fourth-generation leptons and quarks should be stable. In the present letter we examine some consequences of the hypothesis that the lightest fourth-generation lepton is a stable massive neutrino, we show on the basis of the results of our previous works[3–6] that the existing data are consistent with this hypothesis, and we suggest possibilities for checking it experimentally.

Measurements of the width of the Z boson rule out the existence of a fourth neutrino with mass $m<m_Z/2\approx 45$ GeV. For this reason, its admissible mass m must exceed $m_Z/2$. On account of radiative corrections, such heavy neutrinos should contribute to the masses of intermediate bosons, but the effect of at least one additional generation of fermions can be compensated by varying the mass of the top quark within the limits of the experimental error.[7]

Since the fourth-generation charge, whose physical nature we do not specify here, is conserved, the mass of the fourth neutrino cannot be a Majorana mass and must be a Dirac mass. Strict conservation of this charge should also make the fourth neutrino stable.

Assuming for the fourth-generation quarks and leptons the same $SU(3)_c\otimes SU(2)_L\otimes U(1)$ gauge charges as for the corresponding quarks and leptons of the first three generations, the quenched density of the fourth-generation relic neutrinos and antineutrinos can be uniquely calculated on the basis of the theory of a hot universe and the assumption of thermodynamic equilibrium of the plasma for $T>m$, taking account of annihilation effects

$$\nu+\overline{\nu}\to f+\overline{f}, W^+ + W^-,$$

where f is a light fermion.[4]

During the period of formation of the Galaxy, the collisionless gas of massive relic neutrinos is entrained by the baryon matter, and the average cosmological density $\rho_\nu(0)$ of massive neutrinos in the Galaxy increases with increasing baryon density $\rho_b(t)$ as[3,4]

$$\frac{\rho_\nu(t)}{\rho_\nu(0)}\sim\left[\frac{\rho_b(t)}{\rho_b(0)}\right]^{3/4}. \qquad (1)$$

In accordance with the entrainment law (1), massive neutrinos condense predominantly outside the visible region of the Galaxy, and their density increases by 7 to 8 orders of magnitude as compared with the average cosmological density. Such an increase of the neutrino and antineutrino density in the galactic halo can lead to an appreciable effect due their interaction with matter in underground detectors. As we have shown in previous work,[5] the results of the DAMA underground experiment[8] are consistent with such an effect for a neutrino mass of 50 GeV. At the same time, underground experiments rule

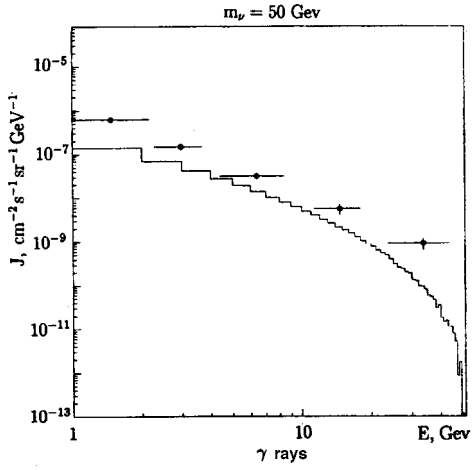

FIG. 1. Comparison of the EGRET data[9] and the results of a simulation of the gamma-ray fluxes from the annihilation of heavy neutrinos with mass $m=50$ GeV in the reactions (2) and (3). The factor by which the neutrino density in the galaxy is enriched over the cosmological neutrino density was taken to be $n_G/n=1.25\times10^7$.

out the range of neutrino masses 60 GeV $<m<$290 GeV.[5] An increase in the neutrino and antineutrino density in the galactic halo results in an appreciable effect due to their weak annihilation, specifically, in the channels

$$\nu+\overline{\nu}\rightarrow e^+ + e^- \tag{2}$$

or

$$\nu+\overline{\nu}\rightarrow q+\overline{q}. \tag{3}$$

Photons form mainly as a result of decays of hadrons arising in the hadronization of quarks and antiquarks in Eq. (3). Numerical calculations of gamma-ray fluxes (see Fig. 1), similar to those performed in Ref. 6, predict for a 50 GeV neutrino mass a galactic gamma-ray background somewhat lower than the EGRET measurements[9] for $E_\gamma>1$ GeV. However, when the inverse Compton scattering of the high-energy electrons and positrons produced in the reaction (2) on galactic optical photons is taken into account,[10] the gamma-ray flux in the energy range 1 GeV$<E_\gamma<$15 GeV increases by (80–40)%, respectively, and leads to agreement with the EGRET data in the region considered. It should also be kept in mind that the EGRET observations of the gamma-ray background with $E_\gamma>50$ GeV indicate the existence of other mechanisms leading to the generation of high-energy gamma rays. Such mechanisms might also contribute in the region $E_\gamma<50$ GeV.

The planned high-precision measurements of the gamma background in the AGILE, AMS, and GLAST experiments can distinguish the sharp cutoff of the photon annihilation spectra at $E_\gamma\approx50$ GeV that is predicted in the present letter.

The present hypothesis of the existence of a fourth neutrino with a mass of about 50 GeV can be checked, for example, in the L3 experiment in the electron–positron collider at CERN by measuring the cross section of the reaction $e^+ + e^- \rightarrow \nu+\overline{\nu}+\gamma$, in which at

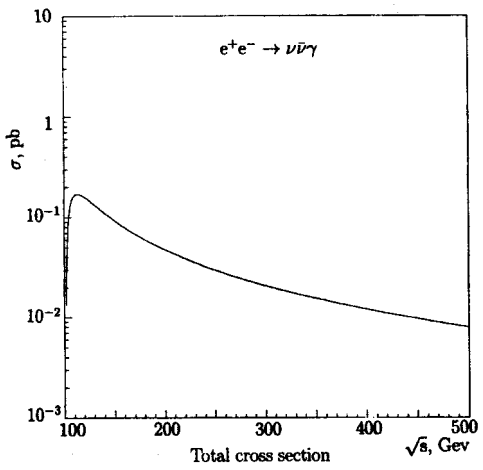

FIG. 2. Total cross section of the process $e^+e^- \to \nu\bar{\nu}\gamma$ for photon energy $\omega > 1.5$ GeV and angles of emergence $30 < \theta < 150°$. The value of M corresponds to the photon energy cutoff $\omega < [(1-4M/s)\sqrt{s}]/2$ for the background process with a massless neutrino.

energies above the mass of the Z resonance only one photon is detected in the final state. Against the background of such a reaction, producing pairs of neutrinos and antineutrinos of the first three generations, the effects due to the formation of a fourth-generation neutrino–antineutrino pair are manifested in a post-threshold increase of the cross section for the production of single photons[11] (see Fig. 2). In accelerator searches for the Higgs meson, if heavy neutrinos exist, then the interesting reaction

$$e^+e^- \to Z\,H \to l^+l^-\nu\bar{\nu},$$

with no hadrons in the final state, can be observed, and this mode could be the dominant mode.

We note that if no new physics appears at scales up to approximately the grand unification scale, then a strong limit on the fourth-neutrino mass $m < 220$ GeV follows from the stability of the electroweak vacuum and from the absence of a Landau pole in the Higgs potential.[7] This likewise shows that it is possible to search for heavy neutrinos in modern accelerator experiments.

The planned experiments on measuring the cosmic-ray fluxes of positrons and antiprotons, specifically, the AMS experiment,[12] make it possible to check directly the existence of a stable neutrino with a mass of 50 GeV. A Monte Carlo calculation, described in detail in Ref. 6, shows (see Figs. 3 and 4) that the expected positron flux from the annihilation reaction (2) could exceed the expected positron cosmic-ray background. By looking for effects due to the reaction (2) one can determine the possible physical nature of an underground detector signal that has not been excluded by the DAMA results. If such a signal is interpreted on the basis of the hypothesis that the neutralino χ a stable, lightest supersymme tric particle, then an appreciable positron signal due to the annihilation of the neutralino in the galactic halo cannot be predicted at the same time. The point is that for a truly neutral particle, which the neutralino should be, a reaction analogous to (2)

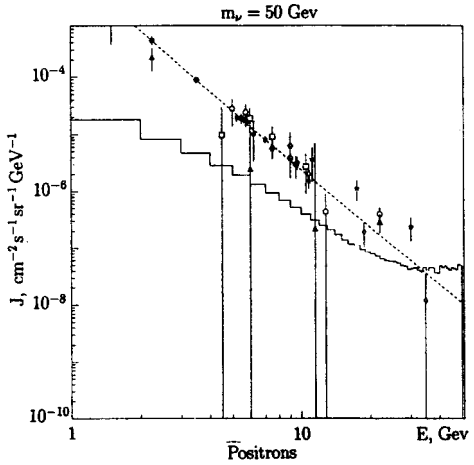

FIG. 3. Simulation results for positron fluxes from the annihilation of heavy neutrinos with mass $m=50$ GeV. Citations to the experimental data are presented in Ref. 6. The enrichment factor for the neutrino density in the galaxy is $n_G/n=1.25\times10^7$.

$$\chi+\chi\rightarrow e^+ + e^- \tag{4}$$

is forbidden in the s wave and can occur only in the p wave.[13] For nonrelativistic neutralinos in the galactic halo $v/c\leqslant10^{-3}$, and the cross section of the reaction (4), which is proportional to $(v/c)^2$, is strongly suppressed.

It is interesting that the methods for checking the present hypothesis in accelerators and in cosmic-ray experiments are complementary. If the dimensionless constant α_{EW}

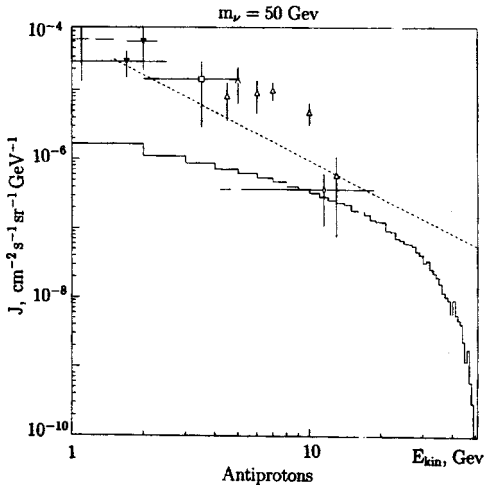

FIG. 4. Simulation results for the antiproton fluxes from the annihilation of heavy neutrinos with mass $m=50$ GeV. Citations to the experimental data are presented in Ref. 6. The enrichment factor for the neutrino density in the galaxy is $n_G/n=1.25\times10^7$.

characterizing the interaction of a fourth neutrino with a Z boson is suppressed, then the pair production of such neutrinos in accelerators will also be suppressed accordingly. At the same time the density of relic neutrinos in the galactic halo is proportional to the quenched density of those neutrinos and inversely proportional to their annihilation rate $r \sim (\sigma v)^{-1}$. The fluxes of the products of annihilation in the reactions (2) and (3) are proportional, going as $F \sim n_\nu n_{\bar{\nu}} \sim r^2(\sigma v) \sim (\sigma v)^{-1} \sim \alpha_{EW}^{-2}$, and therefore the effects of such annihilation intensify as α_{EW} decreases. In the opposite case of increasing α_{EW} these astrophysical effects correspondingly grow weaker, but then it is easier to search for the fourth neutrino using accelerators. We note that at a mass of 50 GeV the neutrino lifetime τ, which is greater than the age of the universe t_U, presumes very strict conservation of the fourth-generation charge. Specifically, the effective dimension-5 operators that would give rise to the decay of such a neutrino as a result of the gravitational interaction, with probability of the form $W \sim m_\nu^3 / m_{Pl}^2$ for $\tau \ll t_U$, should be ruled out.

To advance the present hypothesis it is necessary to analyze the admissible properties of and the possibilities of searching for the effects due to the existence of a stable fourth-generation quark as well as the hadrons of which it could be a constituent. It is of interest to study the possibility of combining the existence of a fourth generation with the horizontal unification model developed earlier.[14] This would still require going beyond the simplest heterotic-string models in which the rank of the symmetry group selected on compactification does not permit including the gauge symmetry of the generations.[15] Combining the indirect experimental, cosmological, and astrophysical control methods should make it possible even in this case to narrow substantially the choice of possible variants of such models.

This work was supported in part by the Kosmion Science and Education Center as part of the division ''Cosmomicrophysics,'' the State Science and Technical Program ''Astronomy. Fundamental Space Research,'' the international project ASTRODAMUS, and the EUROKOS–AMS and Kosmion–ETH Z collaborations. We thank R. Battiston, R. Bernabei, H. Hofer, and A. Starobinskiĭ for fruitful discussions.

*e-mail: golubkov@elma01.npi.msu.su
†e-mail: konoplic@orc.ru
‡e-mail: Roberto.Mignani@roma1.infn.it
§e-mail: Daniele.Fargion@roma1.infn.it
**e-mail: mkhlopov@orc.ru

[1] M. Green, J. Schwarz, and E. Witten, *Superstring Theory*, Cambridge University Press, Cambridge, 1987; Mir, Moscow, 1990.
[2] V. Barger and R. J. N. Phillips, *Collider Physics*, Addison-Wesley, 1988, corrected edition.
[3] Ya. B. Zeldovich, A. A. Klypin, M. Yu. Khlopov, and V. M. Chechetkin, Sov. J. Nucl. Phys. **31**, 664 (1980).
[4] D. Fargion, M. Yu. Khlopov, R. V. Konoplich, and R. Mignani, Phys. Rev. D **52**, 1828 (1995).
[5] D. Fargion, M. Yu. Khlopov, R. V. Konoplich, and R. Mignani, JETP Lett. **68**, 685 (1998).
[6] Yu. A. Golubkov and R. V. Konoplich, Phys. At. Nucl. **61**, 602 (1998).
[7] V. Novikov, http://xxx.lanl.gov/abs/hep-ph/9606318 (1996).
[8] R. Bernabei *et al.*, Nucl. Phys. Proc. Suppl. **70**, 79 (1999).
[9] P. Sreekumar *et al.*, http://xxx.lanl.gov/abs/astro-ph/9709257 (1997).
[10] D. Fargion, R. Konoplich, M. Grossi, and M. Khlopov, http://xxx.lanl.gov/abs/astro-ph/9809260 (1998).
[11] D. Fargion, M. Yu. Khlopov, R. V. Konoplich, and R. Mignani, Phys. Rev. D **54**, 4684 (1996).
[12] H. Hofer and F. Pauss, Grav. Cosm. Suppl. **4**, 56 (1998).

[13] M. S. Turner and F. Wilczek, Phys. Rev. D **42**, 1001 (1990).
[14] A. S. Sakharov and M. Yu. Khlopov, Yad. Phys. **57**, 690 (1994) [Phys. At. Nucl. **57**, 651 (1994)].
[15] Z. G. Berezhiani and M. Yu. Khlopov, Yad. Phys. **51**, 1157 (1990) [Sov. J. Nucl. Phys. **51**, 739 (1990)].

Translated by M. E. Alferieff

Effect of unstable MHD modes on the confinement of a stellarator plasma

D. K. Akulina, G. M. Batanov, M. S. Berezhetskiĭ, G. A. Gladkov, S. E. Grebenshchikov, I. S. Danilkin, L. M. Kovrizhnykh, L. V. Kolik, A. B. Kuznetsov, N. F. Larionova, K. M. Likin, N. I. Malykh, A. I. Meshcheryakov, A. E. Petrov, K. A. Sarksyan, I. S. Sbitnikova, N. N. Skvortsova, D. Yu. Sychugov, O. I. Fedyanin, N. K. Kharchev, Yu. V. Khol'nov, and S. V. Shchepetov
Institute of General Physics, Russian Academy of Sciences, 117942 Moscow, Russia

C. Hidalgo and B. van Milligen
CIEMAT, Madrid

(Submitted 9 February 1999)
Pis'ma Zh. Éksp. Teor. Fiz. **69**, No. 6, 407–412 (25 March 1999)

The results of an experimental study of the influence of unstable MHD modes on plasma confinement in an L-2M stellarator are presented. The spectral and statistical characteristics of turbulent plasma simultaneously at both the edge and center of the plasma are investigated. It is shown that at constant power of electron-cyclotron heating of the plasma the energy content of the plasma depends strongly on the strength of the externally applied vertical magnetic field used to adjust the position of the plasma column. Appreciable degradation of plasma confinement is observed for values of the vertical field such that ideal MHD modes become unstable in the greater part of the plasma column. This in turn is due to the formation of a magnetic configuration with a magnetic ''hump.'' At the same time, in the edge plasma the instability of resistive-balloon modes grows, and turbulent particle transport increases. © *1999 American Institute of Physics.*
[S0021-3640(99)00306-0]

PACS numbers: 52.55.−Hc, 52.35.Bj

1. Substantial efforts have been directed in the last few years to the experimental study of the influence of turbulent processes on plasma confinement,[1] specifically, in stellarator-type magnetic traps (see, for example, Refs. 2–6). However, for the most part either these efforts were directed toward the investigation of global confinement and stability for the purpose of attaining maximum β, which in itself is extremely important, but without a direct connection with the turbulent characteristics of the central part of the plasma column or the experiments were limited to studying turbulent processes in the near-wall plasma. In the present work we posed the problem of determining the degree to which MHD activity at both the edge and center of the plasma column influences plasma confinement. An externally applied vertical magnetic field B_v was selected as the tool for acting on the MHD activity. This field was used to correct the positions of the plasma

column for the Shafranov shift of the magnetic axis and the entire system of magnetic surfaces because of the finite value of β. This choice is not accidental, since for specific fixed values of β for the L-2M stellarator a vertical magnetic field can be used to change the magnetic configuration from a configuration with a magnetic ''well'' to a configuration with a magnetic ''hump,'' where the ideal MHD modes become unstable at the center of the plasma column. Such a formulation of the problem made it necessary to perform measurements of the B_v dependences of the spectral and statistical characteristics of the plasma fluctuations together with the analogous dependences for the macroscopic parameters of the plasma, such as the energy content W, the electron temperature T_e, etc.

In addition to this, it was necessary to measure the fluctuation parameters independently, both at the central and near the periphery of the plasma column. It is obvious that a comparative analysis of the dependences obtained could make it possible to draw conclusions about the effect of (or its absence) MHD activity on plasma confinement. For the central regions one can talk about ideal MHD modes, whereas for the edge plasma, as shown in Ref. 5, these are resistive-balloon modes. Finally we note that wavelet analysis, which has been developed in the last few years, was used to analyze the experimental data. This method makes it possible to obtain information about the spectra and coherence of various spectral components with high time resolution in real-time.[7] The configurations of the magnetic surfaces for the experimental conditions in L-2M stellarator were obtained by studying the plasma equilibrium using the numerical procedure described in Ref. 8.

2. The basic characteristics of the L-2M stellarator are described quite completely in Ref. 9. This is an $l=2$ stellarator with a large shear of the magnetic field and a planar geometric axis, a total number of periods of the helical field $N=14$, a major radius of the torus $R=100$ cm, and an average radius of the vacuum separatrix $r_s=11.5$ cm. The vacuum angle of the rotational transform is $i=0.185$ on the magnetic axis and 0.78 near the separatrix.

A 75 GHz ($\lambda\sim 4$ mm) gyrotron was used to produce and heat a collisionless plasma. The experiments described below were performed at powers 150–200 kW and discharge durations 10–12 ms. For a longitudinal magnetic field $B_0=1.34$ T the resonance condition for electron-cyclotro n resonance at the second harmonic of the gyrofrequency for the extraordinary wave was satisfied for $R=100$ cm. The typical plasma parameters for the present experiments are as follows: average plasma density $n_e\sim(1-2)\times 10^{19}$ m^{-3}, $T_e(0)\sim 0.7$–0.8 keV, and $T_i\sim 0.15$ keV. Hydrogen (H_2) was used as the working gas. The field B_v could be varied in the range $-0.5\%<\epsilon=B_v/B_0<0.5\%$. Fluctuations of plasma density in the hot regions were studied by the phase-contrast method (small-angle scattering) with scattering of the ordinary wave arising as a result of the splitting of the linearly polarized microwave radiation used for electron-cyclotron heating of the plasma. In this case the amplitude of the density fluctuations is proportional to the fluctuations of the radiation intensity.[10]

Mobile Langmuir probes, which are described in detail in Ref. 5, were used to investigate the radial and poloidal structure of the fluctuations and turbulent particle transport at the edge of the plasma column. The thermal energy W of the plasma was measured according to its diamagnetism. The electron temperature T_e and its radial distribution $T_e(r/r_s)$ were measured by the foil method using soft x-ray radiation. In

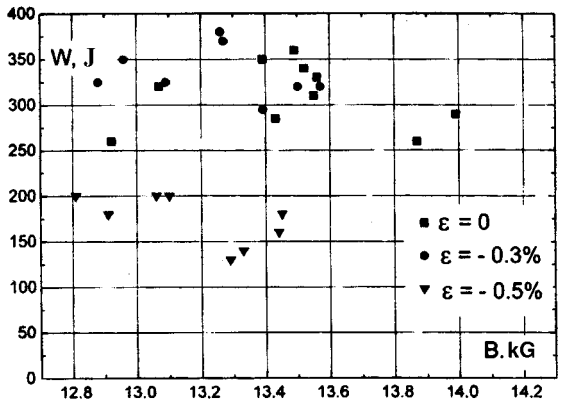

FIG. 1. Thermal energy W of the plasma versus the longitudinal magnetic field B_0.

addition, $T_e(r/r_s)$ was determined from the intensity of the plasma radiation at the second harmonic of the electron gyrofrequency at frequencies 77–80 GHz. A graphite diaphragm was used to decrease the interaction of the plasma with the stainless steel vacuum chamber. In the cases studied the diaphragm was introduced in a manner so as to decrease the average radius of the plasma boundary by 1 cm.

We shall consider the effect of B_v on the plasma density fluctuations at the center of the plasma column for the three cases $\epsilon=0$, $\epsilon=-0.3\%$, and $\epsilon=-0.5\%$. The calculations showed that the $\epsilon=0$ case is stable in ideal MHD because of self-stabilization. For the case $\epsilon=-0.3\%$ there exists a narrow zone where the Mercier stability criterion[11] breaks down at $(r/r_s)\sim 0.5$. For $\epsilon=-0.5\%$ there exist wide zones of instability which encompass virtually the entire central part of the plasma column. Therefore it can be expected for the latter case that the plasma density fluctuations at the center of the plasma column will grow and plasma confinement will be degraded.

We turn now to the results of the measurements, primarily, the diamagnetic measurements of the thermal energy W. Figure 1 shows W versus the longitudinal magnetic field B_0 for three values of B_v: $\epsilon=0$, $\epsilon=-0.3\%$, and $\epsilon=-0.5\%$ for $P_0=170-190$ kW. It is easy to see that for $\epsilon=-0.3\%$ the change in the energy content of the plasma is negligible (the change in the temperature $T_e(0)$ at the center is also negligible). However, increasing B_v to $\epsilon=-0.5\%$, where the Shafranov shift should be completely compensated and where in accordance with the calculations wide MHD instability zones are formed, results in a sharp decrease of the energy content from $W=380$ J at $\epsilon=0$ to $W=180$ J at $\epsilon=-0.5\%$. The electron temperature $T_e(0)$ at the center decreases by a factor of 1.5.

We shall briefly describe the behavior of other plasma parameters when B_v is switched on. The average plasma density n_e and the radiation losses $P_{\rm rad}$ ordinarily increase during a discharge both in the absence of B_v and when the vertical field is switched on. However, when B_v is switched on, the finite values of n_e and $P_{\rm rad}$ increase compared with the regime without B_v. Thus for $\epsilon=-0.5\%$ the average plasma density increases to 2×10^{13} cm^{-3} and $P_{\rm rad}$ increases to 130 kV, while for $\epsilon=0$ it increases to 1.6×10^{13} cm^{-3} and $P_{\rm rad}$ to 80 kW.

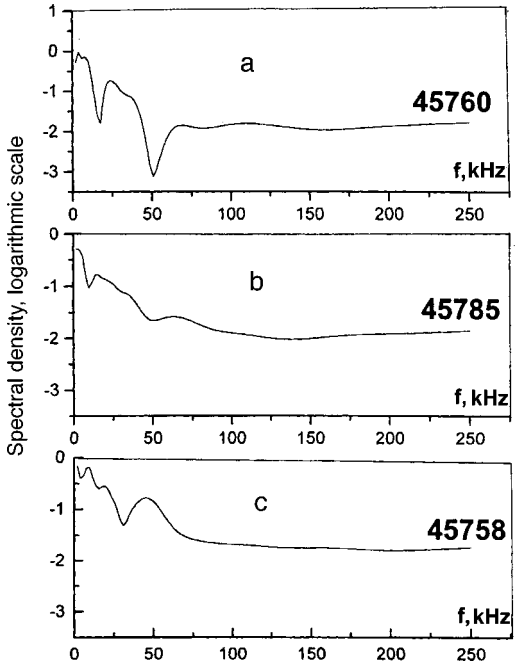

FIG. 2. Wave-packet spectra of the warming radiation transmitted through the plasma column: a) $\epsilon=-0.5\%$, b) $\epsilon=-0.3\%$, and c) $\epsilon=0$.

The characteristics of turbulent plasma fluctuations were measured under the same experimental conditions as for the measurements of W, T_e, and other macroscopic parameters of the plasma. The measurements of the plasma density fluctuations at the center of the plasma column show that the total noise energy increases by a factor of two when the vertical field increases from $\epsilon=0$ to $\epsilon=-0.5$. The corresponding spectra over the wave packets in the absence of a vertical field ($\epsilon=0$) and with partial compensation ($\epsilon=-0.3\%$) and total compensation ($\epsilon=-0.5\%$) of the Shafranov shift are presented in Fig. 2. The spectra in Fig. 2, just as in Fig. 3, were obtained for the same discharge times with averaging over an interval from 1 to 3 ms. For $\epsilon=0$ a noise spectrum that drops off continuously at high frequencies and possesses with a wide band of quasicoherent oscillations at frequencies near 50 kHz and diffuse bands near 10 and 20 kHz is recorded. For $\epsilon=-0.3\%$ redistribution of noise energy over the spectrum is observed: The maximum of the wide band shifts to 60 kHz and a single wide band with a maximum near 15 kHz is recorded at low frequencies. Increasing the vertical field to $\epsilon=-0.5\%$ increases the energy of quasiharmonics in the total noise energy: Two wide bands with peaks of the spectral density near 7.5 and 25 kHz are clearly recorded. The increase in the energy of quasiharmonics with increasing vertical field is also confirmed by the form of the temporal correlations of the functions: Together with the central peak, a large excess of the correlation coefficient above the random noise is recorded at long correlation times (0.1–1 ms).

The calculations of the bicoherence coefficient also show that the nonlinear interaction of the oscillations changes with the vertical field: The bicoherence coefficient in-

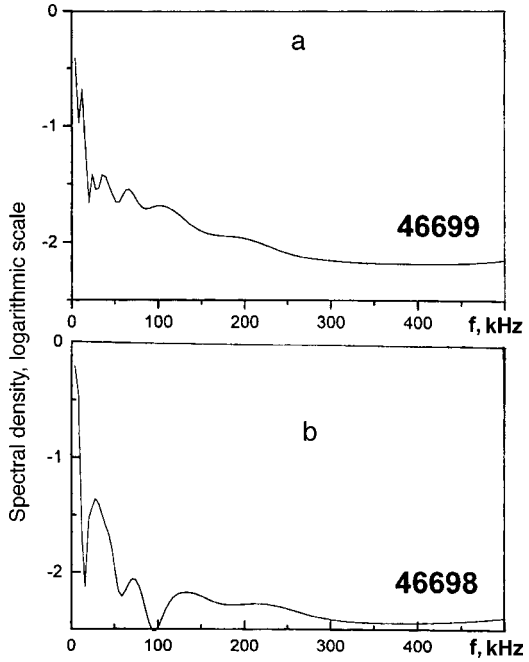

FIG. 3. Wave-packet spectra of the floating potential of a probe in the near-wall plasma ($r/r_s=0.86$): a) $\epsilon=-0.3\%$ and b) $\epsilon=0$.

creases from 0.005 at $\epsilon=0$ to 0.09–0.12 when a vertical field is applied to the plasma column.

Distinct frequency bands are also observed in the wave-packet spectra of the fluctuations of the floating potential in the near-wall plasma. Compensation of the Shafranov shift increases the amplitude of the fluctuations in the entire frequency spectrum in the range where $1\geqslant r/r_s\geqslant 0.86$. In a number of cases the turbulent particle flux increases substantially. As an example, the signals of the radial turbulent particle flux Γ_ω are shown in real time Fig. 4 for $\epsilon=0$ (Fig. 4a) and $\epsilon=-0.3\%$ (Fig. 4b). In the case presented Γ_ω increases by an order of magnitude for $\epsilon=-0.3\%$. Therefore compensation of the Shafranov shift increases the turbulent pulsations of the near-wall plasma and the turbulent particle fluxes.

Comparing the measurements of the scattering spectra of the warming wave and the spectra of the fluctuations of the plasma density and of the floating potential in the near-wall plasma shows that compensation of the Shafranov shift intensifies turbulence both at the center of the column and in the edge plasma. Quasiharmonic structures are formed and a correlation appears between the central and peripheral regions of the column. Since the conditions of instability of resistive MHD modes at the periphery of the plasma column hold for all values of the vertical field, while the ideal MHD modes are stable at the periphery of the column because of the large value of the shear, it is apparently possible to talk about the instability in the central plasma regions influencing the periphery of the plasma.

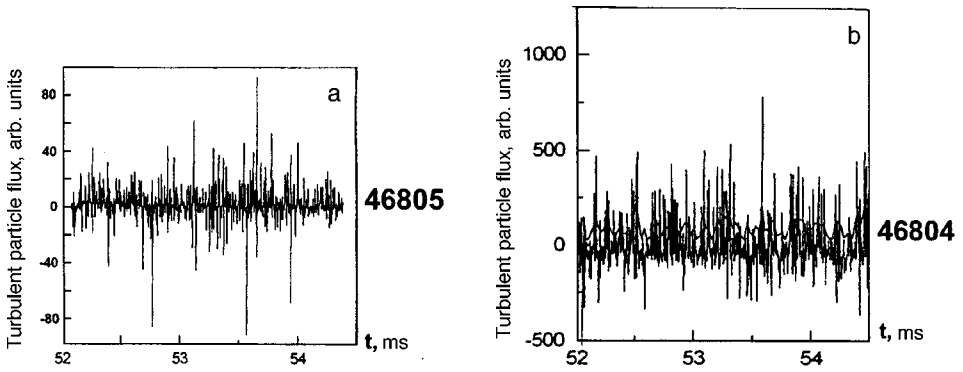

FIG. 4. Radial turbulent particle flux Γ_ω in the near-wall plasma in real-time: a) $\epsilon=0$ and b) $\epsilon=-0.3\%$.

Thus total compensation of the shift of the plasma column because of the finite value of β ($\epsilon=-0.5\%$) results in a strong excess of the instability criterion for ideal MHD nodes over the entire cross section of the column with the exception of its periphery. A two-fold decrease of plasma energy and the electron temperature at the center are recorded. It was established by means of scattering of the wave warming the plasma under these conditions that the energy of the oscillations at the center of the column increases by a factor of two and the quasiharmonic components in their spectrum also increase. The noise and turbulent particle flux in the edge plasma increase at the same time. It can be inferred that the decrease in the energy content is due to the fact that plasma turbulence plays a decisive role in limiting the plasma lifetime in a stellarator.

In conclusion, we wish to report the results of two independent experimental checks of the fact that the degradation of plasma confinement is a consequence of the instability of the MHD modes. The first check concerns the following procedure: One would think that the situation can certainly be improved by decreasing the size of the plasma while leaving constant the vertical field and the heating power by means of a graphite diaphragm. Then the shift of the magnetic surfaces increases and the plasma may turn out to be stable as a result of a deepening of the magnetic well as a result of self-stabilization at the center of the plasma column. It was found that this is indeed the case. Decreasing the average plasma radius to ~ 9 cm did not decrease the thermal energy of the plasma, as would follow from the condition for a quiet plasma. Moreover, the thermal energy of the plasma increased by 20% and the spectrum of density fluctuations turned out to be virtually identical to the case $\epsilon=+0.5\%$ with the same plasma radius.

The second check is associated with the need to eliminate a possible influence of intensified gas liberation from the walls at $\epsilon=-0.5\%$, since calculations show that in this case the extreme closed magnetic surfaces ''settle'' on the chamber walls. For this, at $\epsilon=-0.3\%$, in which case the separatrix does not touch the chamber walls, the gyrotron radiation power was increased to 220–240 kW. It was found that under these conditions $P_{\rm rad}$ and n_e increase to the same values that occur at a lower power but with $\epsilon=-0.5\%$ (the data for $\epsilon=-0.5\%$ were presented above). However, under these conditions the energy content not only did not decrease, but it increased and reached 500–520 J.

It appears that the results of the control experiments also confirm the validity of the conclusions drawn above.

This work was supported by the Russian Fund for Fundamental Research (Grant No. 98-02-16345).

[1] C. Hidalgo, Plasma Phys. Controlled Fusion A **53**, (1995).
[2] J. H. Harris, M. Murakami, B. A. Carreras *et al.*, Phys. Rev. Lett. **63**, 1249 (1989); Phys. Fluids B **2**, 1353 (1990).
[3] O. Motojima, F. Sano, M. Sato *et al.*, Nucl. Fusion **25**, 1783 (1985).
[4] S. Okamura, K. Matsuoka, K. Nishimura *et al.*, Nucl. Fusion **35**, 283 (1995).
[5] G. M. Batanov, O. I. Fedyanin, N. K. Khartchev *et al.*, Plasma Phys. Controlled Fusion **40**, 1241 (1998).
[6] M. A. Pedrosa, C. Hidalgo, and B. van Milligen, Plasma Phys. Controlled Fusion **38**, 365 (1996).
[7] N. N. Astaf'eva, Usp. Fiz. Nauk **166**, 1145 (1996).
[8] S. V. Shchepetov and A. B. Kuznetsov, Usp. Fiz. Nauk **36**, 1097 (1996).
[9] V. V. Abrakov, D. K. Akulina, E. D. Andryukhina *et al.*, Nucl. Fusion **37**, 233 (1997).
[10] A. G. Zhukovskiĭ, *Plasma Density Fluctuations* [in Russian], Énergoatomizdat, Moscow, 1983.
[11] L. M. Kovrizhnykh and S. V. Shchepetov, Fiz. Plazmy **6**, 576 (1980) [Sov. J. Plasma Phys. **6**, 533 (1980)].

Translated by M. E. Alferieff

Induced emission from a sodium Rydberg atom in a microwave cavity

I. M. Beterov and I. I. Ryabtsev*

Institute of Semiconductor Physics, Siberian Branch of the Russian Academy of Sciences, 630090 Novosibirsk, Russia

(Submitted 25 January 1999)
Pis'ma Zh. Éksp. Teor. Fiz. **69**, No. 6, 413–416 (25 March 1999)

Results are presented from an experiment on the observation of an induced microwave transition $37P-37S$ in sodium Rydberg atoms under the action of 30 thermal photons in a microwave cavity. The measured value of the transition rate $(4\pm1.5)\times10^4$ s^{-1} agrees with the calculated value. © *1999 American Institute of Physics.* [S0021-3640(99)00406-5]

PACS numbers: 32.30.Bv, 32.80.Rm

Thermal radiation has a large effect on the lifetimes of Rydberg states,[1] since the low frequencies of the transitions between them lie in the region of the emission spectrum of a blackbody at any temperature. Since the dipole moments of Rydberg atoms are very large, a strong coupling with the radiation arises, and transitions are induced to low-lying levels after one Rydberg state has been excited. As a result, the populations of the levels are redistributed, and for high-lying states with principal quantum number $n\geqslant20$ the lifetime decreases appreciably in comparison with the radiative lifetime. When the atoms are placed in a cavity, the rates of individual transitions under the action of thermal photons can increase substantially because the spectral density of the electromagnetic field oscillators increases near a transition.[2]

The rate of induced transitions between two Rydberg states under the action of a thermal-photon field in a cavity which has a quality factor Q and effective volume $V_{\rm eff}$ and is tuned to the transition frequency ω is described by the expression[2]

$$\Gamma=\Gamma_0\bar{n}\eta, \tag{1}$$

where $\Gamma_0=8\pi^2d^2/3\epsilon_0\hbar\lambda^3$ is the rate of spontaneous transitions (d is the matrix element of the dipole moment and λ is the wavelength) in free space, $\bar{n}=1/[\exp(\hbar\omega/kT)-1]$ is the average number of thermal photons per mode of the electromagnetic field at the resonance frequency with cavity temperature T, and the factor $\eta=3Q\lambda^3/4\pi^2V_{\rm eff}$ reflects the change in the density of oscillators (in a cavity there is one oscillator for the frequency interval $\Delta\omega_{\rm eff}=\pi\omega/2Q$ and the photon lifetime is $\tau=Q/\omega$).

The effect of thermal radiation with temperature 100 K on the rate of the microwave transition $37P_{3/2}$–$37S_{1/2}$ (frequency 70.166 GHz) in sodium Rydberg atoms (Fig. 1a) was investigated experimentally. The spectrum of this transition and the behavior of the

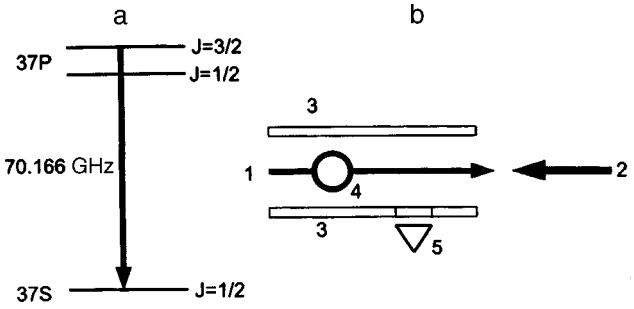

FIG. 1. a) Microwave transition $37P$–$37S$ in sodium Rydberg atoms. b) Experimental arrangement: *1* — Na beam, *2* — laser radiation, *3* — copper plates, *4* — microwave cavity, *5* — channel multiplier.

spectrum in a static electric field were studied in detail in Ref. 3. The $37P$ state possesses fine structure (114 MHz).

The experimental arrangement is displayed in Fig. 1b. Sodium atoms in an effusion beam with temperature 500 K were excited into Rydberg states by the three-step scheme $3S$–$3P$–$4S$–$37P_{J=1/2,3/2}$ with counterillumination of the beam in the longitudinal direction by radiations from three synchronized pulsed tunable lasers with repetition period 200 μs and pulse durations 20–100 ns. Rydberg atoms in the $37P$ state appeared with a uniform density along the entire beam. The velocity distribution of atoms corresponded to a Maxwellian distribution with average velocity 700 m/s. The populations of the Rydberg levels were monitored by selective field ionization in a pulsed electric field between two copper plates. The electrons produced as a result of ionization were detected with a vacuum channel multiplier, and the signal from the output of the multiplier was processed in a pulse-counting mode in a CAMAC crate and a computer. The delay in switching on the electric field relative to the laser pulses ranged from 8 to 160 μs, which made it possible to detect selectively atoms which at the moment of laser excitation were located in different parts of the beam, including also in the microwave cavity 30 mm from the detector.

A 9.6 mm in diameter tunable cylindrical copper cavity operating in the mode H_{115} with $\Omega \approx 7000$ and $V_{\text{eff}} \approx 0.5$ cm^3 was used. The atomic beam was passed through the center of the cavity perpendicular to the cylindrical face. The electric component of the field in the cavity possesses a maximum at this point and remains essentially unchanged along the beam. The H_{115} mode is doubly degenerate with respect to the polarization of the radiation. The weak ellipticity of the cavity cross section lifted the degeneracy of the cavity. The cavity and all components of the detection system were cooled with liquid nitrogen to 100 K, which corresponds to $\bar{n} \approx 30$ in one cavity mode. It can be determined from the known parameters of the cavity that $\eta \approx 80$, i.e., the rates of the spontaneous and stimulated transitions should be 80 times higher for a tuned cavity.

The dipole moment of the transition $37P_{3/2}$–$37S_{1/2}$ can be calculated in the semiclassical approximation[4] and is $d = 680ea_0$ for transitions with $\Delta M_J = 0$ with linearly polarized microwave radiation. Hence follows the computed value $\Gamma_0 = 12$ s^{-1}, and the total transition rate in free space at 100 K is $\Gamma' = \Gamma_0 + \Gamma = 370$ s^{-1}. The transition probability over a characteristic delay time $t \approx 100$ μs is $W_1 = \Gamma' t = 0.04$ with a detuned

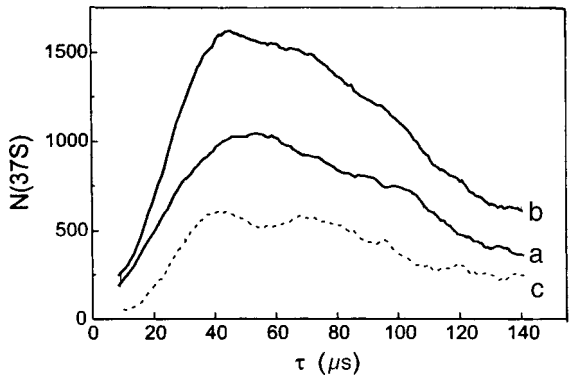

FIG. 2. Number of atoms in the 37*S* state versus the delay time after the laser pulse: a) with a detuned cavity, b) with the cavity tuned to the frequency of an atomic transition, and c) difference of the curves a and b, corresponding to a change in the signal only as a result of the interaction with thermal photons.

cavity. Therefore, in this case the effect of thermal photons on the transition rate can be neglected. For a tuned cavity $\Gamma' = 3 \times 10^4\ \mathrm{s}^{-1}$, and over the average transit time of atoms through the cavity (15 μs) the transition probability $W_2 \approx 0.4$ is high, so that the increase in the population of the $37S_{1/2}$ state is due mainly to atoms which have passed through the cavity. Atoms interact weakly with thermal photons before entering and after leaving the cavity.

It should be noted that the computed free-space lifetimes of the 37*P* and 37*S* states, taking account of the effect of thermal radiation[1] and transitions to all other levels, are 150 and 50 μs, respectively. This must be taken into account when measuring populations with a delay after the laser pulse. In addition, collisions of Rydberg atoms with residual-gas molecules in the vacuum chamber can appreciably affect transition rates. Analysis shows that in our experiment in the case of a detuned cavity the appearance of a signal from atoms in a 37*S* state with increasing delay of the ionization pulse (Fig. 2a) is due to collisions, since, as we have already seen, the probabilities of transitions under the action of thermal photons are low in this case. For short delays the signal is observed to grow linearly, and for long delays the signal decreases on account of the decay of the initial 37*P* state. The vertical scale of the plot corresponds to the average number of Rydberg atoms in the 37*S* state that are detected over 1000 laser pulses in the counting mode, taking account of the transparency of the grid of the channel multiplier and the nonlinearity of the signal. A numerical fit of the dependence in Fig. 2a gave the absolute rate $(1.5 \pm 0.3) \times 10^4\ \mathrm{s}^{-1}$ for the collision-induced transition $37P-37S$.

Tuning the cavity to the transition frequency resulted in a large increase of the signal for delay times greater than 30 μs (Fig. 2b). This time corresponds to the transit time to the detector for atoms that were present in the cavity at the moment of laser excitation. Therefore the observed change, as compared with Fig. 2a, in the signal is determined by the atoms that have passed through the cavity containing thermal photons and that have undergone an induced transition from the 37*P* state into the 37*S* state. Figure 2c shows the difference of the curves a and b, which represents the change in the signal only as a result of the interaction with thermal photons in the cavity. This dependence was also fit numerically taking account of the velocity distribution of the atoms in the beam and the

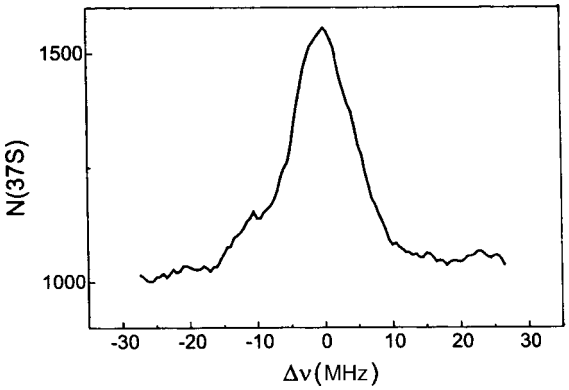

FIG. 3. Number of atoms in the 37*S* state versus the detuning of the cavity frequency with a 50 μs delay.

lifetimes of the *S* and *P* states. This made it possible to extract the experimental value of the absolute rate of transitions induced by thermal photons $(4\pm1.5)\times10^4$ s^{-1}, which is close to the computed value.

The transition spectrum was recorded with a fixed delay of 50 μs. The tuning frequency of the cavity was adjusted continuously near the transition frequency and the signal from atoms in the $37S_{1/2}$ state was measured (Fig. 3). The width of the resonance was determined primarily by the cavity *Q* (10 MHz), since the natural width of the transition (4 kHz) and the Doppler width (200 kHz) were small. The observed change in the signal amplitude near resonance characterizes the increase in the rate of thermal-photon-induced transitions as compared with the rate of collision-induced transitions, and in addition the radiative decay of atoms in the 37*S* state after the atoms have left the cavity must be taken into account. Actually, the present experimental arrangement implements a high-sensitivity narrow-band detector of thermal and microwave radiations with a sensitivity at the level of several photons.

In conclusion, we note the following. In the present experiment the $37P_{3/2}$ and $37S_{1/2}$ states form a two-level system which is completely inverted initially. A downward transition is accompanied by the emission of a photon into a cavity mode. If the number of initially excited atoms inside the cavity is sufficiently large, collective phenomena of the type Dicke superradiance and maser generation of microwave radiation at the frequency of an atomic transition can arise.[5] Preliminary estimates show that for the existing parameters of the experiment about 100 inverted atoms in the cavity are required to observe this effect. At the same time, in our experiments this number did not exceed 10, and superradiance can be neglected. Plans are now being made to observe this effect by increasing the density of Rydberg atoms. It is also of definite interest to observe zero-threshold generation and amplification without inversion in a Rydberg micromaser with coherent pumping according to the scheme proposed in Ref. 6 and to investigate the influence of thermal photons on its properties.

We thank D. B. Tret'yakov, a student at the Novosibirsk State Technical University, for assisting in the experiments and the analysis of the results. This work was supported by grants from the Russian Fund for Fundamental Research (Grants Nos. 96-02-19041 and 97-02-18551).

*e-mail: ryabtsev@isp.nsc.ru

[1] T. F. Gallagher, in *Rydberg States of Atoms and Molecules*, edited by R. F. Stebbings and F. B. Dunning, Cambridge University Press, New York, 1983; Mir, Moscow, 1985, p. 194.
[2] E. M. Purcell, Phys. Rev. **69**, 681 (1946).
[3] I. M. Beterov and I. I. Ryabtsev, JETP Lett. **68**, 897 (1998).
[4] A. R. Edmonds, J. Picart, N. Tran-Minh, and R. Pullen, J. Phys. B **12**, 2781 (1979).
[5] L. Moi, P. Goy, M. Gross *et al.*, Phys. Rev. A **27**, 2043 (1983).
[6] N. Lu, Phys. Lett. A **143**, 457 (1990).

Translated by M. E. Alferieff

Acoustic analog of the Fermi resonance

M. I. Katsnel'son
Institute of Metal Physics, Urals Branch of the Russian Academy of Sciences, 620219 Ekaterinburg, Russia

A. P. Platonov and A. V. Trefilov
Kurchatov Institute Russian Science Center, 123182 Moscow, Russia

(Submitted 21 December 1998; resubmitted 1 February 1999)
Pis'ma Zh. Éksp. Teor. Fiz. **69**, No. 6, 417–422 (25 March 1999)

It is shown that for acoustic waves in crystals nonlinear phenomena of a new type, analogous to some degree to Fermi resonance in molecules, can occur. It is demonstrated on the basis of an analysis of the numerical solution of the equations of motion that for propagation of waves with different polarization and with sound velocities in integral ratio, the energy transfer from one wave to another is of the nature of beats with quite low amplitudes and can become chaotic as the amplitudes increase. © *1999 American Institute of Physics.*
[S0021-3640(99)00506-X]

PACS numbers: 43.25.Dc, 43.25.Gf, 62.65.+k

It is well known that in crystal-lattice dynamics anharmonic effects (AEs) lead to a shift of the frequency and damping of phonons.[1,2] It is natural to expect the appearance of qualitatively new features primarily in the cases where for some vibrational modes the potential is strongly anharmonic, for example, double-well.[3–5] New branches of elementary excitations, e.g., solitons,[3] can appear, additional ''zero-phonon'' peaks will appear in the inelastic neutron scattering spectrum,[5] and so on. However, the conventional picture may also be inadequate for weak AEs with ''resonant'' ratios of the phonon frequencies at certain points of the Brillouin zone.[6–8] Such a situation is apparently realized for high-symmetry points in phonon spectra of a number of metals, for example, for the bcc phase of alkaline and alkaline-earth metals — at the point (2/3, 2/3, 2/3).[6] To some degree it is analogous to the ''Fermi resonance'' well known in molecular physics.[9,10] However, for metals the classical limit $T \gg \hbar\omega$ (where ω is the characteristic phonon frequency and T is the temperature) is primarily of interest. This limit is much richer than the ultraquantum limit that is realized for molecules consisting of light atoms and that was studied by Fermi. Specifically, in the classical limit there arises a nontrivial low-frequency dynamics (quasistatic displacements) that is associated with energy transfer between the modes participating in the resonance. The present letter is devoted to an analysis of AEs accompanying the interaction of sound waves whose sound velocities are in integral (resonant) ratio (thus far an interaction of this kind has been studied only between oscillators and not waves propagating in space). Passing to this case opens up new possibilities for the experimental investigation of the corresponding nonlinear reso-

nant phenomena, since it is much easier to change the amplitude, phase, and other important characteristics for acoustic waves than for phonons with finite wave vectors.

Formally, the problem of the interaction of waves differs substantially from the problem of the interaction of individual oscillators by the fact that it is necessary to solve a system of partial differential equations in the former case and ordinary differential equations in the latter case. Of course, in the numerical solution the partial differential equations are reduced to a system of ordinary differential equations, but their number increases substantially.

We shall indicate first the real objects where the ''acoustic Fermi resonance'' situation can occur, i.e., the sound velocities are in integral ratio. It is quite simple to give examples of crystals with 1:1 and 1:3 ratios of the sound velocities. In both cases the waves are transverse acoustic waves propagating in the $\langle 110 \rangle$ direction in cubic crystals, where $c_1 : c_2 = \sqrt{C'/C_{44}}$ and C' and C_{44} are two independent shear moduli. Examples of such crystals are alkaline metals near the melting point, where $C'/C_{44} \approx 1/9$ and $c_1 : c_2 = 1/3$, and the alloys $W_{1-x}Re_x$ and $Mo_{1-x}Re_x$, where $C' \approx C_{44}$ for small x. We investigated in greater detail the 1:1 model. The corresponding Lagrangian density can be written in the form

$$L = 1/2(\dot{u}^2 + \dot{v}^2) - 1/2(u'^2 + v'^2) - Au'^2 v'^2 + 1/2D(u'^4 + v'^4), \tag{1}$$

where $u(t,x)$ and $v(t,x)$ are the displacements of the waves. An overdot indicates a derivative with respect to the time t and a prime indicates a derivative with respect to the spatial coordinate x. We took account of anharmonic terms describing the simplest AEs of the ''intermode'' (A) and ''intramode'' (D) types. For the calculations periodic boundary conditions $u(x+L) = u(x)$ and $v(x+L) = v(x)$, where L is the size of the ''crystal'' being modeled, were employed and the x derivatives were replaced by finite differences. The initial conditions were chosen in the form of simple sinusoidal waves with different random phase shifts between the u and v waves, and the initial maximum values of $|u'|$ and $|v'|$ were taken to be 1.

The behavior of the system for various values of the interaction constants is illustrated by the results presented in Figs. 1–4 (the behavior of $u(t)$ with fixed x is shown; it follows from the calculations that the behavior of $u(x)$ for fixed t is similar). For $A < 10^{-3}$ beats arise between the u and v waves. These beats are quasiperiodic, as is evident from the phase portraits. We underscore that these beats are a purely nonlinear effect, since we are studying the case of strictly equal wave velocities. Then the main peak in the spectrum of sound velocities (frequencies) splits at a velocity equal to 1. This splitting is is the analog of the splitting of the frequencies of oscillators at a Fermi resonance.[10] As the intermode anharmonic coupling constant A increases, the main peak in the Fourier spectrum becomes wider and overtones appear near integral values of the velocity. For large values of A energy ''transfer'' between the u and v waves becomes chaotic, and the points in the phase portrait fill part of the phase space more or less uniformly and, correspondingly, the Fourier spectrum becomes wide-band. This behavior is insensitive to the intramode coupling constant D, as follows from the general qualitative analysis in Ref. 7 of the role of various anharmonic terms. We also note that the picture remains qualitatively the same for not too large detuning of the velocities.

Analogous calculations were also performed for the 1:3 model with the Lagrangian density

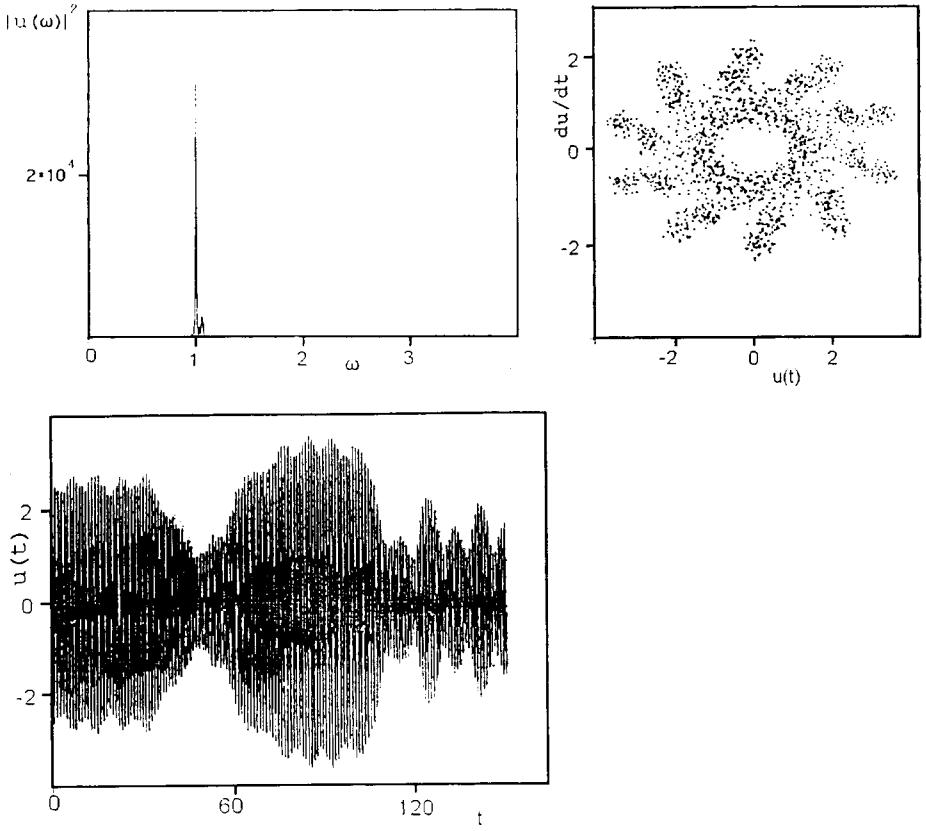

FIG. 1. Phase portrait $(du/dt,u)$ for $v=0$, the spectral power $|u_\omega|^2$, and the function $u(t)$ for $A=5\times10^{-4}$ and $D=2\times10^{-4}$. The frequency is measured in units of $\omega_0=q_0$, where q_0 is the wave number of a sinusoid at $t=0$.

$$L=1/2(\dot{u}^2+\dot{v}^2)-1/2(u'^2+9v'^2)-Au'v'^3, \tag{2}$$

where only the ''resonant'' anharmonic terms responsible for intermode energy transfer with weak anharmonicity are retained. The behavior was found to be qualitatively similar to that investigated for the 1:1 model. We note that the instability of sinusoidal waves for almost all initial conditions in the model (2) can be proved analytically.[7]

Experimentally, the resonant interaction of acoustic waves could be observed by exciting the waves in appropriate crystals (examples of which were presented above). When the sound velocities deviate substantially from integral ratios when the temperature or impurity concentration is varied, the picture should simplify substantially, reducing to ordinary ''linear'' beats. Apparently, the splitting of the sound velocities can also be observed in inelastic neutron scattering experiments, where it is manifested as an anomalously strong broadening of the corresponding branches of the phonon spectrum in the acoustic region. However, here we are dealing with thermal vibrations and there arises the question of the effect of the interaction with the thermostat on the phenomena described here. For the case of a resonant interaction of oscillators, according to Ref. 8,

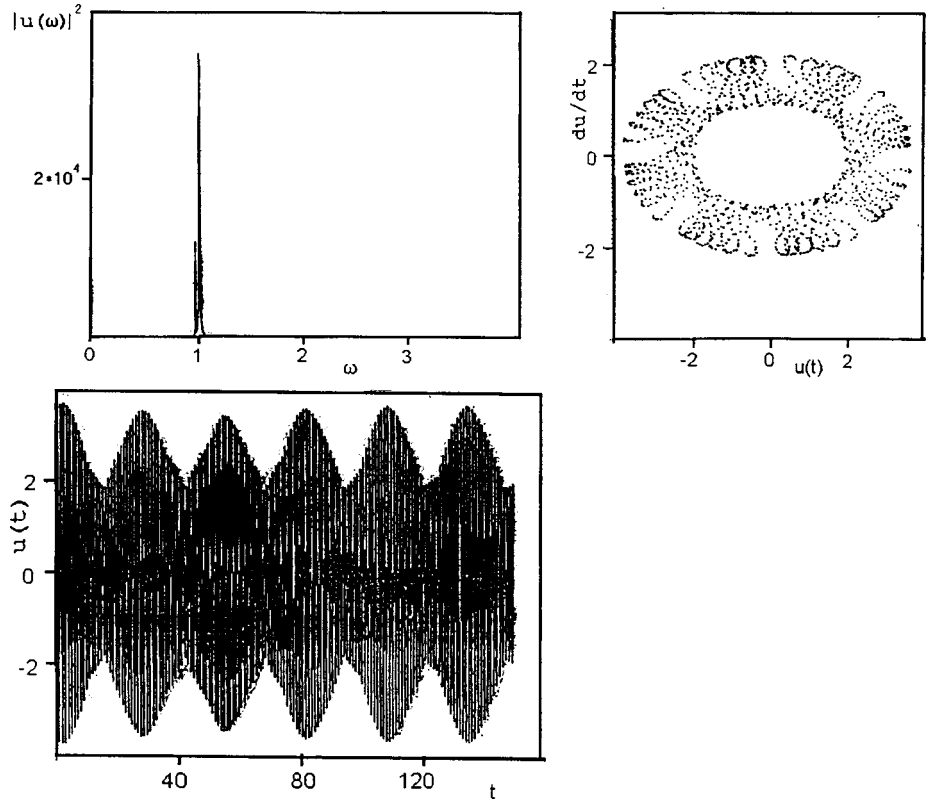

FIG. 2. Same as Fig. 1 for $A=5\times10^{-4}$ and $D=-10^{-3}$.

thermal noise does not destroy the Fermi resonance, though the picture becomes more complicated. The picture of intermode energy transfer and instability of the sinusoidal waves certainly remains complicated when the interaction with the thermostat is taken into account. Qualitative considerations of the possible role of the ''resonant'' instability of sound waves in the melting scenario have been discussed in Ref. 7. It would be interesting to check them by including thermal noise in the models investigated here. Then there arises a methodologically nontrivial problem of solving stochastic partial differential equations. Our preliminary results show that the results obtained here remain qualitatively valid when the interaction with the thermostat is taken into account.

In closing, we shall briefly consider the question of the possibility of observing experimentally the effects predicted in this letter. The specific vibrational regime for the crystals discussed, i.e., the character of the energy transfer, depends on the amplitude of the vibrations and the magnitude of the detuning of the corresponding sound velocities. For definiteness, we shall examine in greater detail the case of a 1:1 resonant ratio of the sound velocities, which occurs, for example, for transverse acoustic waves propagating in the $\langle 110\rangle$ direction in crystals of the alloys W–Re and Mo–Re. Depending on the rhenium concentration, the ratio of the sound velocities can be both somewhat greater and somewhat less than 1; the scale of the ratio C'/C_{44} and therefore the ratio of the squared

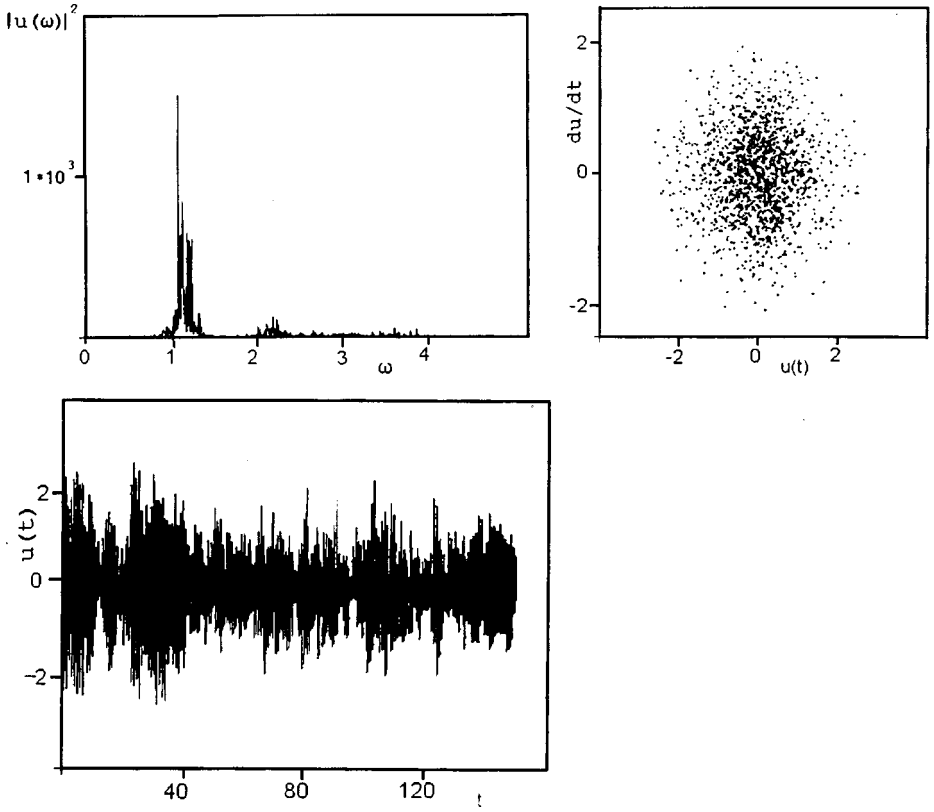

FIG. 3. Same as Fig. 1 for $A=5\times10^{-3}$ and $D=0$.

corresponding sound velocities is of the order of 15% with the rhenium concentration in these alloys in the interval $0\leqslant x\leqslant 0.2$.[11] The scale of variation of C'/C_{44} with temperature increasing from room temperature up to the melting point with a fixed concentration is of the same order of magnitude ($\approx 10\%$).[11] Therefore fine tuning of this ratio can be accomplished by varying the temperature. Then the resonance phenomena considered here will be observed in a certain interval of detuning, and for the largest detuning a transition will occur to a regime of ordinary linear beats. It can be expected, by analogy to the model for oscillators whose frequencies are in the ratio 1:2 (Refs. 6 and 8), that the critical detuning of the velocities should be of the order of several percent. Then the experiment would consist of exciting simultaneously two transverse waves with different polarization and investigating the transfer of energy between them, for example, by measuring the corresponding spectral characteristics for each wave as a function of their amplitude, determined by the external perturbation, and as a function of the velocity detuning. Similarly, a 1:3 velocity ratio can be obtained, i.e., the ratio of the shear moduli $C'/C_{44}\approx 1/9$ for these sound waves in single crystals of alkali metals near the melting point (see Ref. 7); in this case the detuning can be accomplished by lowering the temperature.

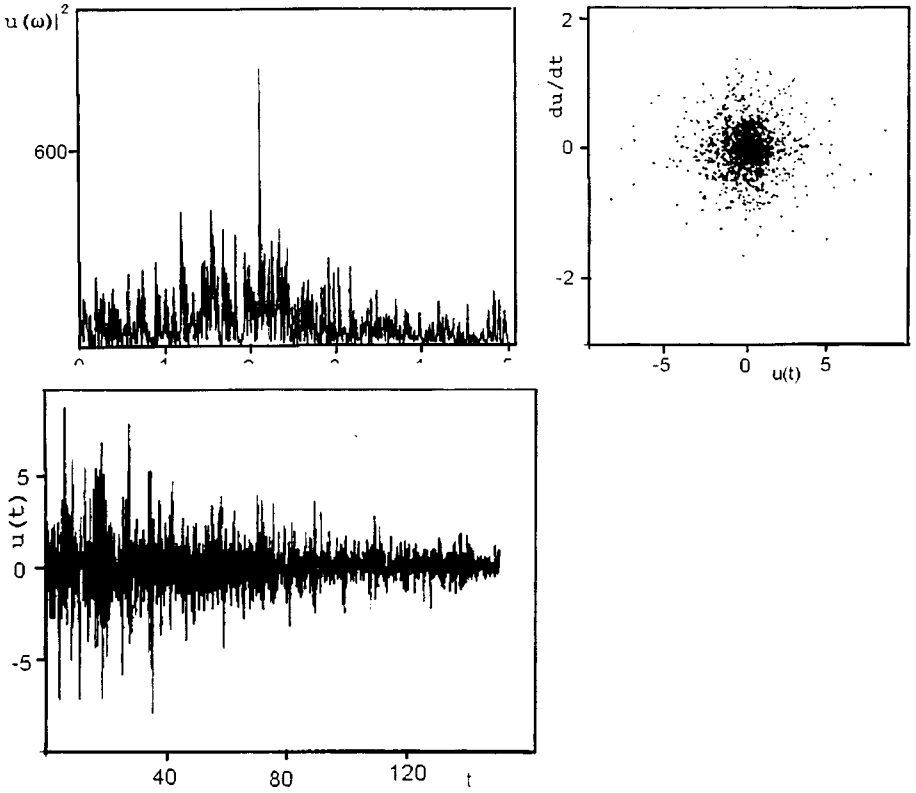

FIG. 4. Same as Fig. 1 for $A=0.5$ and $D=0$.

This work was supported by the Russian Fund for Fundamental Research (Grant No. 98-02-16219).

[1] R. A. Cowley, Adv. Phys. **12**, 421 (1963).
[2] V. G. Vaks, S. P. Kravchuk, and A. V. Trefilov, Usp. Fiz. Nauk **155**, 159 (1988) [Sov. Phys. Usp. **31**, 474 (1988)].
[3] J. A. Krumhansl and J. R. Schrieffer, Phys. Rev. B **11**, 3535 (1975).
[4] K.-M. Ho, C. L. Fu, and B. N. Harmon, Phys. Rev. B **29**, 1575 (1984); Y.-Y. Ye *et al.*, Phys. Rev. Lett. **58**, 1769 (1987).
[5] Yu. N. Gornostyrev, M. I. Katsnel'son, and A. V. Trefilov, JETP Lett. **56**, 529 (1992); Yu. N. Gornostyrev, M. I. Katsnelson, A. V. Trefilov, and S. V. Tret'jakov, Phys. Rev. B **54**, 3286 (1996).
[6] M. I. Katsnel'son and A. V. Trefilov, JETP Lett. **45**, 634 (1987); Zh. Éksp. Teor. Fiz. **97**, 1892 (1990) [Sov. Phys. JETP **70**, 1067 (1990)].
[7] M. I. Katsnel'son and A. V. Trefilov, Fiz. Met. Metalloved. **64**, 629 (1987).
[8] Yu. N. Gornostyrev, M. I. Katsnel'son, A. P. Platonov, and A. V. Trefilov, (1995) JETP Lett. **80**, 525 (1995); Phys. Rev. B **51**, 12817 (1995).
[9] E. Fermi, Z. Phys. **71**, 250 (1931).
[10] M. P. Lisitsa and A. M. Yaremko, *Fermi Resonance* [in Russian], Naukova Dumka, Kiev, 1984.
[11] Yu. N. Gornostyrev, M. I. Katsnelson, A. V. Trefilov, and R. F. Sabiryanov, Phys. Met. Metallogr. **74**, 421 (1992).

Translated by M. E. Alferieff

Mechanism of the transport of nickel along a Si(111) surface in the presence of adsorbed cobalt atoms

A. E. Dolbak, B. Z. Ol'shanetskiĭ,* and S. A. Tiĭs
Institute of Semiconductor Physics, Siberian Branch of the Russian Academy of Sciences, 630090 Novosibirsk, Russia

(Submitted 8 February 1999)
Pis'ma Zh. Éksp. Teor. Fiz. **69**, No. 6, 423–425 (25 March 1999)

The mechanism of the transport of nickel along a Si(111) surface in the presence of adsorbed cobalt atoms is established by LEED and Auger electronic spectroscopy. The mechanism consists of diffusion of nickel atoms through the bulk and segregation of the atoms on the surface during annealing. This mechanism of nickel transport plays the governing role at temperatures below 700 °C, where nickel transport along clean silicon surfaces is not observed. It is found that the nickel segregation factor is what determines the lowest temperature at which nickel transport is observed on clean silicon surfaces.
 [S0021-3640(99)00606-4]

PACS numbers: 68.35.Fx

Surface diffusion is the basis of many processes occurring on solid surfaces.[1,2] Even though surface diffusion has been studied comparatively little experimentally, existing data attest to a great diversity of physical processes participating in the transport of atoms along a crystal surface. According to existing ideas, the migration velocities of atoms on a surface are higher and the diffusion activation energy is lower than the corresponding quantities in the bulk of a solid, i.e., the diffusion of atoms on a surface should occur more easily than in the bulk. But it is found that this is not always the case. To advance the understanding of surface diffusion it is of interest to follow the behavior of Ni on silicon surfaces. Investigations using LEED and Auger electron spectroscopy (AES) have shown that Ni transport along initially clean Si surfaces proceeds not by surface diffusion but rather by the diffusion of Ni through the bulk of Si followed by segregation on the surface as a result of a decrease of the solubility of Ni in Si as temperature decreases.[3] This conclusion is based on the absence of an Ni signal in the Auger spectra from the surface of a silicon sample undergoing annealing. The Ni concentration distributions which are formed as a result of diffusion appear only after the sample temperature has decreased. Nickel transport on clean Si surfaces can be observed by AES at temperatures above 700 °C. At lower temperatures the sensitivity of LEED and AES was found to be inadequate for detecting the Ni distributions obtained because the solubility of Ni in Si (see, for example, Ref. 4) and the Ni surface segregation factor decrease.

It has been observed recently that in the presence of submonolayer concentrations of adsorbed Co[5] and Fe[6] atoms the temperature range where transport on an Si surface is

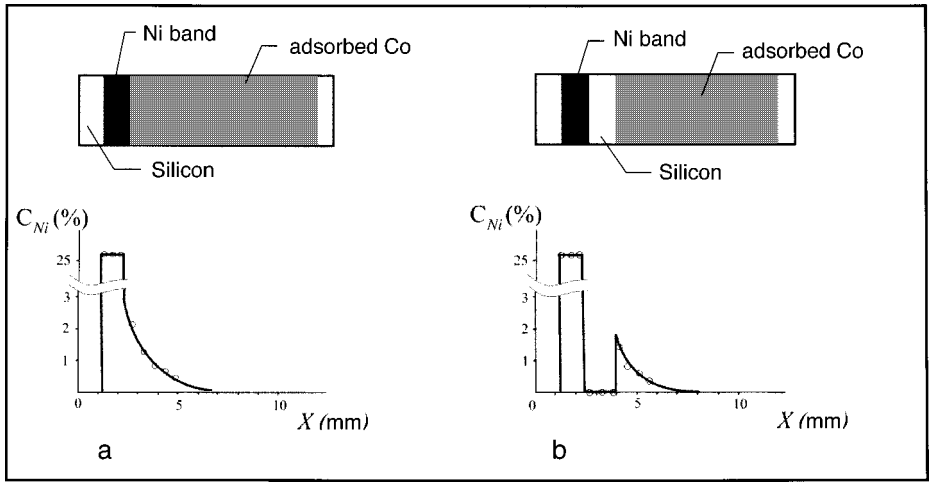

FIG. 1. Experimental arrangement. Top — diagram of the sample: a) a nickel strip is deposited on a silicon surface containing adsorbed Co; b) a nickel source lies at some distance from the section containing an adsorbed coating. Bottom — form of the corresponding surface nickel concentration distributions C_{Ni}, x — distance from the edge of the nickel strip.

observed expands substantially in the direction of lower temperatures, specifically, to 500 °C on a surface with adsorbed Co and 600 °C on surface with adsorbed Fe. Moreover, in contrast to a clean surface, in these experiments the Ni Auger signal is observed even during annealing of the sample in the process of diffusion of Ni, i.e., an additional mechanism of nickel transport appears in the presence of atoms of a second metal. The computational results for the corresponding diffusion coefficients of nickel and the temperature dependence of these coefficients are presented in Refs. 5 and 6. However, the mechanism of Ni transport on an Si surface with adsorbed atoms of a second metal has remained unknown. In the present work we established the nature of this mechanism on the basis of experimental results obtained by using LEED and AES to study nickel transport on a Si(111) surface in the presence of adsorbed Co atoms.

Two mechanisms can be proposed for Ni transport for which Ni will be detected by AES on an Si surface during annealing of the sample. The first one is surface diffusion associated with adsorbed atoms of a second metal present on the surface. In the second one adsorbed metal atoms can promote surface segregation of Ni atoms diffusing through the bulk during annealing of the silicon sample.

To determine which of these mechanisms occurs we proceeded as follows. A coating consisting of 0.4 monolayers of Co was deposited on the clean surface of a sample with Si(111) — 7×7 structure and an Ni strip with a sharp boundary, serving as a source for the diffusion of Ni atoms, was deposited. In some experiments the boundary of the Ni strip was located on a section of the surface containing adsorbed Co (Fig. 1a), while in other experiments this strip was deposited 1.5 mm from the edge of the region with the adsorbed Co coating (Fig. 1b). This was accomplished using collimation of atomic beams. Next the samples were heated at 640 °C, at which temperature Ni transport on a clean Si surface is not detected. The nickel concentration distributions C_{Ni} along the sample were measured by AES. The form of these distributions is shown in Figs. 1a and

1b. If Ni diffusion had occurred on the surface, then the Ni concentration distributions should not be observed in the experiment with the scheme for Fig. 1b, since at 640 °C the Ni atoms would not be able to overcome the distance between the Ni strip and the section with adsorbed Co. Therefore Ni transport on an Si surface with adsorbed Co is due to Ni diffusion through the bulk and segregation on the surface, which occurs during annealing of the sample. This explains the possibility of detecting Ni by AES on an Si surface during diffusion.

The contribution of the described mechanism to Ni transport decreases with increasing temperature. Nickel could be detected on an Si surface with adsorbed metal atoms at temperatures up to 900 °C, but above 700 °C the same mechanism as on a clean Si surface, i.e., Ni diffusion through the bulk of Si and segregation of Ni on the surface as temperature decreases, makes the main contribution to Ni transport on such surfaces.

In summary, at temperatures below 700 °C Ni transport along an Si surface with adsorbed Co atoms occurs by a mechanism based on the diffusion of Ni atoms through the bulk of Si and segregation of Ni atoms on the Si surface during the diffusion process. It can also be concluded from the experimental results that the lowest temperature at which Ni transport can be observed on clean Si surfaces is determined not by the quantity of Ni diffusing through the bulk but rather by the Ni surface segregation factor.

This work was supported by the Russian Fund for Fundamental Research (Grant No. 98-02-17843) and the Government Scientific and Technical Program ''Surface Atomic Structures'' (Project No. 2.2.99).

*e-mail: olshan@isp.nsc.ru

[1] B. I. Boltaks, *Diffusion and Point Defects in Semiconductors* [in Russian], Nauka, Leningrad, 1972.
[2] Ya. E. Geguzin and Yu. S. Kaganovskiĭ, *Diffusion Processes on Crystal Surfaces* [in Russian], Énergiya, Moscow, 1984.
[3] A. E. Dolbak, B. Z. Olshanetsky, S. I. Stenin *et al.*, Surf. Sci. **218**, 37 (1989).
[4] Eicke R. Weber, Appl. Phys. A **30,** 1 (1983).
[5] A. E. Dolbak, B. Z. Ol'shanetskiĭ, S. A. Tiĭs *et al.*, JETP Lett. **66**, 643 (1997).
[6] A. E. Dolbak, B. Z. Olshanetsky, and R. A. Zhachuk, Phys. Low-Dim. Struc. **9/10**, 97 (1998).

Translated by M. E. Alferieff

Effect of the anticrossing of excitonic states on their phase relaxation time in a GaAs/AlGaAs symmetric double quantum well

K. L. Litvinenko* and V. G. Lysenko

Institute of the Technology of Microelectronics and Ultrapure Materials, Russian Academy of Sciences, 142432 Chernogolovka, Moscow Region, Russia

(Submitted 9 February 1999)
Pis'ma Zh. Éksp. Teor. Fiz. **69**, No. 6, 426–430 (25 March 1999)

The change in the properties of excitonic states near anticrossing is investigated experimentally. It is shown that the phase relaxation time of light excitons in a GaAs/AlGaAs symmetric double quantum well increases by a factor of five as a result of mixing of the energy states of light and heavy excitons. © *1999 American Institute of Physics.* [S0021-3640(99)00706-9]

PACS numbers: 73.20.Dx, 68.65.+g, 71.35.−y

In the last few years there has been a great deal of interest in the investigation of various properties of excitonic states in quantum wells, double quantum wells, and superlattices. The purpose of these investigations is to study fundamental processes in quantum-size structures for the purpose of devising new principles of operation of various electrooptic devices.[1–3] Special attention is devoted to the investigation of the effect of an external constant electric field whose flux lines are parallel to the direction of growth of the experimental structures. There have been quite a few experimental and theoretical works[4–6] on the change in the wave functions and energies of excitonic states in an external field. Anticrossing, a well-known effect in quantum mechanics, has been predicted and experimentally observed in double quantum wells[6–9] and superlattices.[10] However, the change in the dynamic properties of excitonic states near anticrossing has not been adequately studied. In the present letter we shall show for the phase relaxation time of excitonic states near anticrossing that mixing of the wave functions results in a large change in the properties of the excitonic states participating in the interaction.

The interaction between quantum wells separated by a quite thin barrier has the effect that the degenerate energy states split into symmetric and antisymmetric.[11] Symmetric states have a lower energy, and we shall label them with a minus sign; antisymmetric states will be labeled with a plus sign. Besides the basic symmetric and antisymmetric states of electrons E, heavy holes HH, and light holes LH, in what follows we shall consider the first excited state HH_1 of heavy holes. Thus eight of the indicated energy states lead to 12 possible optical transitions, which we shall designate by numbers from 1 to 12:[11] Transition 1 corresponds to the recombination of an electron $E_{(-)}$ and a hole $HH_{(-)}$; 2 — $E_{(-)}$ and $HH_{(+)}$; 3 — $E_{(-)}$ and $LH_{(-)}$; 4 — $E_{(-)}$ and $LH_{(+)}$; 5 — $E_{(-)}$ and $HH_{1(-)}$; 6 — $E_{(-)}$ and $HH_{1(+)}$; 7 — $E_{(+)}$ and $HH_{(-)}$; 8 — $E_{(+)}$ and

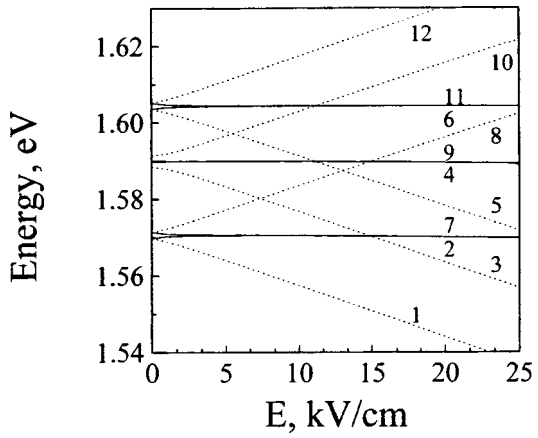

FIG. 1. Electron-hole optical transition energies as a function of the intensity E of the applied external electric field for the SDQW used in the experiment (see text for explanations).

$HH_{(+)}$; 9 — $E_{(+)}$ and $LH_{(-)}$; 10 — $E_{(+)}$ and $LH_{(+)}$; 11 — $E_{(+)}$ and $HH_{1(-)}$; and 12 — $E_{(+)}$ and $HH_{1(+)}$. The transitions 1, 3, 6, 8, 10, and 11 are optically allowed in a zero external field, while the transitions 2, 4, 5, 7, 9, and 12 are forbidden.[11,12] When a nonzero external electric field is applied, the selection rules change, and previously allowed transitions become forbidden. If energy is measured from the center of the double quantum well, then the symmetric (antisymmetric) energy states will move in the direction of decreasing (increasing) energy with increasing external field intensity.[11] The symmetric (antisymmetric) electronic and hole states lie in different quantum wells. The result is that the overlap of the symmetric (antisymmetric) electron and hole wave functions, which is proportional to the probability of an optical transition between these states, decreases. The probability of optical transitions between symmetric and antisymmetric states increases as a result of the shift of these states in identical quantum wells.

A variational method was used to determine the change in the energies of optical transitions between electronic and hole states in an external electric field.[9] The results of calculations performed for a symmetric double quantum well (SDQW) used in the experimental part of the present work are presented in Fig. 1. As the external field increases, the energy positions of some transitions cross. This occurs because, as we have already mentioned above, the symmetric and antisymmetric hole states move in different directions on the energy scale. However, the real situation is somewhat more complicated. As the external field increases, the crossing energy states do not pass through one another as they cross, but rather they mix and seemingly change places. We shall examine this effect for the states $HH_{(+)}$ and $HH_{1(-)}$. Figure 2 shows the change in the normalized wave function of the $HH_{(+)}$ state at a transition through a resonant value of the external field ($E_{\rm res}\approx 26.55$ kV/cm), for which crossing of the levels $HH_{(+)}$ and $HH_{1(-)}$ should be observed. At a sufficient distance from $E_{\rm res}$ the wave function is essentially a pure $HH_{(+)}$ state. However, as the external field increases, the energy states start to mix and the wave function acquires a new form. The maximum mixing occurs in an external field equal to $E_{\rm res}$. As the field increases further, the contribution of the $HH_{1(-)}$ state in the mixed state obtained increases and even for an external field greater than $E=26.8$ kV/cm we see

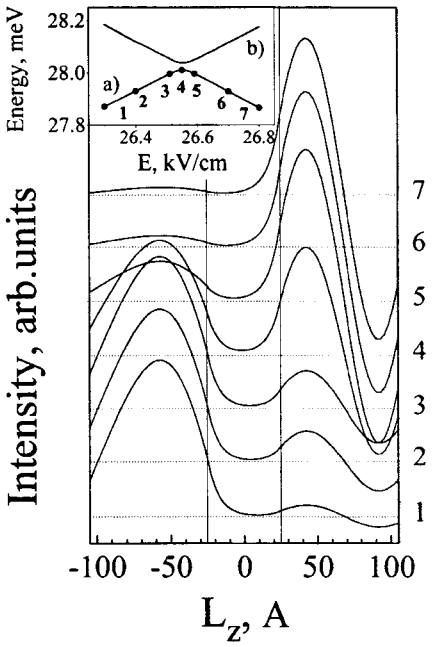

FIG. 2. Variation of the form of the wave function of the $HH_{(+)}$ state in the case of anticrossing with the $HH_{1(-)}$ state for electric field intensities E indicated in the inset. The vertical lines indicate the boundaries of the quantum wells.

an essentially pure $HH_{1(-)}$ state. As a result of mixing, the properties of the energy state that before the transition through E_{res} corresponded to $HH_{(+)}$ gradually change and the state passes into the state $HH_{1(-)}$. The inset in Fig. 2 shows the variation of the energy of the $HH_{(+)}$ level at the transition through E_{res}. Thus the properties of the second interacting energy level $HH_{1(-)}$ also change.

To investigate experimentally the change in the properties of mixed (in the case of anticrossing) excitonic levels we used a GaAs/AlGaAs SDQW with an 80 Å wide well and a 50 Å wide barrier, and we used the four-wave mixing (FWM) method with spectral resolution.[13] A tunable titanium–sapphire laser with 120 fs pulses was used as the source of laser radiation. The intensity of the FWM signal decreases exponentially with a characteristic decay time T as the delay time increases. The phase relaxation time T_2 is related with T as $T_2 = Tn$, where $n = 1/2$ for a homogeneously broadened level and $n = 1/4$ for inhomogeneous broadening.[14] In the present work we do not distinguish between homogeneous and inhomogeneous broadening of the experimentally observed excitonic lines, since the ratio of these two factors in the anticrossing region differs appreciably from their ratio for pure excitonic states. This is the subject of our subsequent investigations. Figure 3a shows the energy positions of excitonic lines observed in the spectrum of the FWM signal with zero delays for applied voltages from 1 to 3 V. These lines correspond to the electron–hole transitions 4, 5, 8, and 9 shown in Fig. 1. The displacement of excitonic lines relative to the computed electron–hole transitions makes it possible to estimate the binding energy of the excitons, which in our experiment was approximately 8.8 meV. The intensities of the coinciding excitonic lines, which corre-

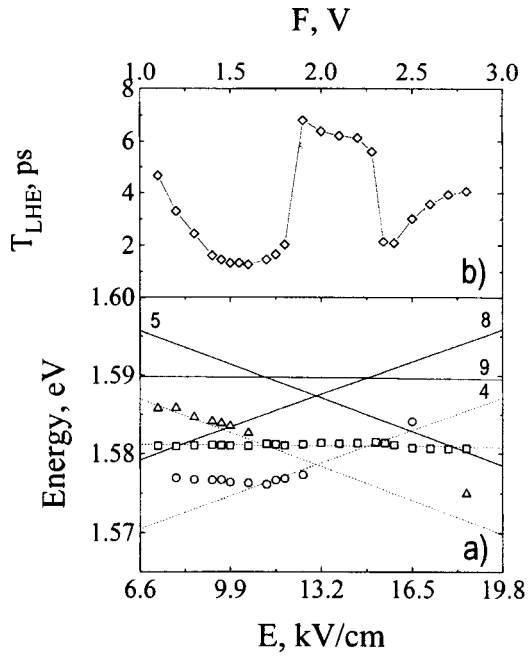

FIG. 3. a) Positions of the maxima of the lines observed in the spectrum of the FWM signal of the experimental structure with zero delays for different values of the intensity F of the external electric field. The solid lines indicate the positions of the corresponding electron–hole transitions (see Fig. 1). b) Decay time of the FWM signal of light excitons (4 and 9) as a function of the intensity E of the external field.

spond to the transitions 4 and 9, are much greater than the intensities of the other lines (5 and 8), which are observed independently in the FWM signal spectrum only near zero delays. The position of the excitonic line 8 at low electric-field intensities is shifted in the direction of high energies. This is due to the fact that the spectrum of excited states in the FWM signal is determined by the product of the distribution of the excitonic states by the spectrum of the exciting laser radiation. The energy of the maximum of the laser radiation spectrum was chosen to be the same as the position of the excitons 4 and 9, and its width was approximately 25 meV.

Figure 3b shows the decay time T_{LHE} of the FWM signal versus the strength of the external electric field for the combined light-exciton lines (4 and 9). As the field intensity increases, T_{LHE} decreases, and passes through a minimum ($T_{LHE} \approx 1.3$ ps) near anticrossing of the light-exciton lines with the exciton 5. Then T_{LHE} remains constant, until it once again starts to decrease and reaches its second minimum near anticrossing of light excitons with the exciton 8. Since the light-exciton lines are optically resolved, their phase relaxation time is much longer than that of excitons 5 and 8. We find from Fig. 3b the average value for the unperturbed light-exciton level $T_{LHE} \approx 6.5$ ps for values of F ranging from 1.9 to 2.2 V. The decrease in the value of T_{LHE} in anticrossing regions can be explained by mixing of light- and heavy-exciton states, similarly to the mixing, studied above, of the heavy-hole states $HH_{1(-)}$ and $HH_{(+)}$. Even though the selection rules forbid optical transitions with the participation of the heavy excitons 5 and 8, mixing with the light-exciton states substantially increases the probabilities of these transitions. As the

electric field intensity approaches the value $F_{\mathrm{res}}^{(\mathrm{exc})} \approx 13$ kV/cm (see Fig. 3), beats are observed in the FWM spectrum of the light excitons. The period of these beats corresponds exactly to the energy splitting between the light excitons and the exciton 5. As the external field increases, the probabilities of the transitions 5 and 8 decrease superlinearly,[11,15] so that in the region of anticrossing of light excitons with the exciton 8 virtually no beats are observed and the decrease in the phase relaxation time is less than in the first case.

In summary, it has been shown in this letter that the phase relaxation time of light excitons decreases by at least a factor of five as a result of mixing of the wave functions of these states with the wave functions of optically forbidden heavy excitons. This confirms the conjecture that the properties of excitonic states change substantially in the anticrossing region. It is important to note that the change occurs when the external electric field increases by only 0.3 V (from 1.7 to 2.0 V).

This work was supported by the GKNT fund (Grant No. 97-1058) and the Russian Fund for Fundamental Research (Grants Nos. 97-02-16833 and 98-02-16153).

*e-mail: kostja@ipmt-hpm.ac.ru

[1] Doyeol Ahn, IEEE J. Quantum Electron. **QE-25**, 2260 (1989).
[2] Yasunori Tokuda, Kyozo Kanamoto, and Noriaki Tsukada, Appl. Phys. Lett. **56**, 166 (1990).
[3] D. A. Miller, J. S. Weiner, and D. S. Chemla, IEEE J. Quantum Electron. **QE-22**, 1816 (1986).
[4] M. M. Dignam and J. E. Sipe, Phys. Rev. B **43**, 4084 (1991).
[5] Tsuneo Kamizato and Mitsuru Matsuura, Phys. Rev. B **40**, 8378 (1989).
[6] Yasunori Tokuda, Kyozo Kanamoto, Yuji Abe, and Nokiaki Tsukada, Phys. Rev. B **41**, 10280 (1990).
[7] K. Leo, J. Shah, E. O. Gobel *et al.*, Phys. Rev. Lett. **66**, 201 (1991).
[8] D. A. B. Miller, D. S. Chemla, T. C. Damen *et al.*, Phys. Rev. B **32**, 1043 (1985).
[9] A. M. Fox, D. A. B. Miller, G. Livescu *et al.*, Phys. Rev. B **44**, 6231 (1991).
[10] P. M. Young, H. Ehrenreich, P. M. Hui, and N. F. Johnson, J. Appl. Phys. **74**, 7369 (1993); T. Meier, G. von Plessen, P. Thomas, and S. W. Koch, Phys. Rev. Lett. **73**, 902 (1994).
[11] W. L. Bloss, J. Appl. Phys. **67**, 1421 (1989).
[12] Y. J. Chen, E. S. Koteles, B. S. Elman, and C. A. Armiento, Phys. Rev. B **36**, 4562 (1987).
[13] J. Erland and I. Balslev, Phys. Rev. A **48**, R1765 (1993).
[14] C. Dornfeld and J. M. Hvam, IEEE J. Quantum Electron. **QE-25**, 904 (1989).
[15] J. Lee, M. O. Vassell, E. S. Koteles, and B. Elman, Phys. Rev. B **39**, 10133 (1989).

Translated by M. E. Alferieff

Twisting of α-quartz tetrahedra at pressures near the transition to the amorphous state

S. V. Goryaĭnov and N. N. Ovsyuk
Institute of Minerology and Petrography, Siberian Branch of the Russian Academy of Sciences, 630090 Novosibirsk, Russia

(Submitted 5 January 1999; resubmitted 10 February 1999)
Pis'ma Zh. Éksp. Teor. Fiz. **69**, No. 6, 431–435 (25 March 1999)

It is found that the main contribution to the distortion of α-quartz tetrahedra at high pressures is their twisting. It is shown that torsional vibrational modes lead to an instability that gives rise to amorphization of the structure. © *1999 American Institute of Physics.* [S0021-3640(99)00806-3]

PACS numbers: 62.50.+p, 81.40.Vw

Many computer calculations of the structure of α-quartz at high pressures have been performed in the last few years.[1–4] Such calculations take account of the distortion of the tetrahedra, such that the interactions between various structural parameters become numerous and complicated and the particular parameters responsible for the basic mechanisms leading to the deformation of the structure remain obscure. To determine these mechanisms we propose a simple valence-force model in which only the two structural parameters that are most pressure-sensitive stand out. One such parameter was found in previous work — the rotation angle of the SiO_4 tetrahedra, which is usually employed for describing the $\alpha-\beta$ transition in quartz.[5] This angle is the main parameter of the deformation of the structure at high pressures, and it is thought that it can lead to an instability that gives rise to amorphization.[6] We have found another parameter by analyzing the numerous deformation parameters presented in the literature for the deformation of tetrahedra. We noticed that they can be reduced to a single parameter — the angle of twist, which has not been previously considered as an order parameter at high pressures. We determine the angle of twist as the deviation from the 90-degree angle between two opposite symmetric edges of tetrahedra in α-quartz. As a result, we were able to find the characteristic features that remained unnoticed in the numerical calculations, specifically, that the rotation angle at high pressures approaches saturation and that the angle of twist, conversely, starts to vary nonlinearly and is therefore the parameter that is mainly responsible for structural instability. This information is important, since despite a number of experimental and theoretical investigations of the amorphization of quartz under pressure,[1–9] there is still no detailed description of such a transition.

The models developed previously for explaining high-temperature anomalies cannot be used to describe the process of amorphization of α-quartz,[10–13] since they neglect the large distortions of the tetrahedra. In our valence-force model of the deformation of α-quartz, which takes account of the distortion of the tetrahedra, the parameters related

with the smallest force constants and therefore vary most strongly with pressure play the main role. For example, if the main force constants are considered, then the constant of the Si–O bonds is much larger than the force constant of the O–Si–O angles, and the latter constant is much greater than the force constant of the Si–O–Si angles. For this reason, for our model we employ as the key parameters the rotation angle, which is related with the force constant of the Si–O–Si angle, and the angle of twist, which is responsible for deformation inside tetrahedra and is related with the force constant of the O–Si–O angles. To give a complete description of the structure of quartz it is necessary to introduce four additional parameters — two symmetric O–Si–O angles and two Si–O bond lengths. According to the experimental data, these four parameters are virtually pressure-independent at high pressures,[14] and for this reason we shall assume them to be constant. All parameters are relative and are measured from the parameters of ideal β-quartz with the Si–O distance equal to 1.5993 Å . A calculation using existing experimental structural data[14] shows that even at pressures above 3 GPa the rotation angle φ is approximately 100 times greater than the four parameters mentioned above, and the angle of twist τ, describing the distortion of the tetrahedra, is approximately 10 times greater than these small parameters. Therefore, in what follows we shall use only the angle of twist to describe the distortion of tetrahedra.

Ordinarily, only the rotation angle is used to construct an analytical model of the deformation of the structure of quartz.[5,10] We shall examine the Gibbs potential, which, besides the rotation angle, also takes account of the angle of twist:

$$G = 3K_\theta[(\theta_0 - \theta) - (\theta_0 - \theta_m)]^2 + 3K_s\tau^2 + (P_\alpha + P)v, \tag{1}$$

where $v = (V - V_0)/V_0$ is the relative change in the unit-cell volume, θ is the Si–O–Si angle, and K_θ and K_s are the force constants (in GPa) of the Si–O–Si and O–Si–O angles, respectively. Here we neglect the small off-diagonal force constants. The quantity P_α is the internal pressure that converts the β-quartz structure isothermally into the α-quartz structure.[15] This potential takes into account the strain arising in the α-quartz structure as a result of the fact that the Si–O–Si angle at which there is no deformation is $\theta_m = 147°$ while the corresponding angle in ideal β-quartz is $\theta_0 = 155°$. Using the expansion of V and θ in terms of the parameters φ and τ, we obtain the Gibbs potential whose variable part has the form

$$\Delta G = K_\tau\tau^2/2 + K_\varphi\varphi^2/2 - g_1\tau + g_2\tau\varphi^2 + g_4\varphi^4, \tag{2}$$

where all coefficients are linear functions of pressure. The equilibrium values of φ and τ for the minimum of this potential are

$$\varphi = [(-K_\varphi - 2g_1g_2/K_\tau)/(4g_4 - 2g_2^2/K_\tau)]^{1/2}, \tag{3}$$

$$\tau = (g_1 - g_2\varphi^2)/K_\tau. \tag{4}$$

Using these equations, we shall construct the functions $\varphi(P)$ and $\tau(P)$ displayed in Figs. 1 and 2. Analyzing the function $\varphi(P)$ at high pressures, we find that it approaches saturation as a result of the contribution of the coefficient g_4, which increases linearly with pressure. Previously, this saturation was presumed on the basis of experimental data,[14] but it was never substantiated. It should be noted that the saturation of the rotation angle with increasing pressure is due to an increase of its effective stiffness $K^*_{\varphi\varphi} = \partial^2\Delta G/\partial\varphi^2$, which attests to an increase in the stability of the structure and cannot be

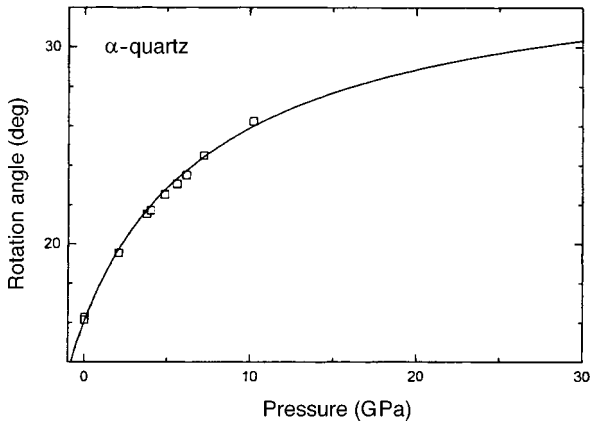

FIG. 1. Rotation angle φ of SiO_4 tetrahedra in α-quartz versus pressure, calculated using Eq. (3). The squares show the experimental data of Ref. 14; at higher pressures, for trigonal quartz the silicon and oxygen coordinates have not yet been determined.[16]

attributed to the onset of instability. It is evident from the pressure dependence $\tau(P)$ that at high pressures the angle of twist of tetrahedra starts to grow nonlinearly, and therefore the effective stiffness of the angle of twist $K^*_{\varphi\varphi}=\partial^2\Delta G/\partial\tau^2=K_\tau$ and, with it, certain other elastic moduli decrease, and an instability giving rise to a disordered structure can arise. To check this hypothesis we performed calculations of the lattice dynamics. These calculations were performed not with the interatomic potentials, as is ordinarily done, but rather using the valence-force field. This approach makes it possible to obtain the pressure dependence of the force constants in an explicit form. The force field of an α-quartz crystal is described in Ref. 17 using the scaled force constants $K^0_{q_i,q_j}$ of molecular silicate clusters calculated by quantum-chemical methods.

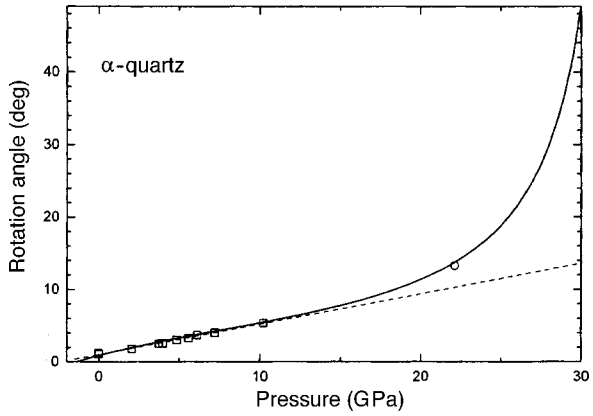

FIG. 2. Angle of twist τ of SiO_4 tetrahedra in α-quartz versus pressure, calculated using Eq. (4). The squares show the experimental data of Ref. 14. The circle at 22 GPa shows the average angle of twist τ_{A_1} for the triclinic phase, calculated using the structural data of Ref. 19. For clarity, the dashed curve shows the linear dependence.

In our calculations we employed the indicated force constants, to which, in order to take the pressure into account, we added the second derivatives of the term PV in the Gibbs potential with respect to the normal coordinate q_i about the equilibrium positions of the atoms, determined by the parameters $\varphi(P)$ and $\tau(P)$ from Eqs. (3) and (4). A similar procedure was performed in Ref. 18. As a result we obtained the pressure-dependent effective stiffnesses of the normal coordinates

$$K^*_{q_i,q_j} = K^0_{q_i,q_j} - P(\partial^2 V/\partial q_i \partial q_j).$$

The low-frequency transverse acoustic mode in the direction $[\xi,\xi,0]$ in the Brillouin zone was calculated using these effective stiffnesses and the matrix of the kinematic coefficients, which are pressure-dependent. It was found that the velocity of an acoustic wave near the point Γ is determined by the torsional stiffness $\nu \sim (K^*_{\tau E_1,\tau E_1})^{1/2}$ (where the parameter τ_{E_1} is discussed below) and approaches zero with increasing pressure. The form of these soft acoustic oscillations is a sum of the amplitudes of the torsional transverse wave, which mainly entails displacements of the oxygen atoms, and an acoustic transverse wave, in which it is primarily the Si atoms that are displaced. This softening can give rise to the appearance of imaginary frequencies of the torsional modes and therefore instability of the tetrahedra with respect to twisting and then to amorphization.

It was recently ascertained that, according to experimental[16] and theoretical[19] investigations, a triclinic phase forms at 21 GPa prior to amorphization. Calculation of the coordination of the atoms in this phase showed that one of the three Si atoms in a cell is in fivefold coordination, very close to that described in Ref. 20. Thus at a triclinic transition some Si atoms are transferred into a fivefold coordination. The torsional oscillations in the soft modes described above can lead to such a transition. We shall determine the particular parameters that are responsible for the transition to the triclinic phase.

Each of the three tetrahedra of a cell in α-quartz has one degree of freedom associated with twisting. Three degrees of freedom give rise to different twisting τ_1, τ_2, and τ_3 of the three tetrahedra in a cell in α-quartz; this gives rise to three torsional parameters $\tau_{A_1} = (\tau_1 + \tau_2 + \tau_3)/3$, $\tau_{E_1} = (\tau_2 - \tau_1)/2$, and $\tau_{E_2} = \tau_3 - \tau_1/2 - \tau_2/2$, which contain static and dynamic components. The static part determines the equilibrium parameters of the structure, and the dynamic part determines the vibrations about these equilibrium positions, which make a contribution with a definite amplitude to the normal modes of the crystal. The static part of the average angle τ_{A_1} was previously defined as the twist. The static parts τ_{E_1} and τ_{E_2} are zero in α-quartz and nonzero in the triclinic phase. Our calculations, using structural data for the triclinic phase,[19] showed that the main torsional parameter is τ_{E_1}. This parameter leads to the same increase of the angle τ_2 and decrease of the angle τ_1, so that the average angle τ_{A_1} continues to fall on the curve in Fig. 2. The soft modes giving rise to a transition to the triclinic phase contain the symmetry-breaking shear modes, which contain a large contribution from the *E*-type torsional vibrations as well as from the longitudinal modes, which are responsible for the volume deformation of the cell to which the A_1-type torsional vibrations contribute. The transition to the triclinic phase strongly intensifies the amorphization process, since because of symmetry breaking the torsional parameter τ_{A_1} contributes not only to the bulk modulus but also to the shear modulus, sharply decreasing it. Amorphization of this new triclinic structure occurs with a further increase of the pressure above 21 GPa. In view of the fact that x-ray diffraction

analysis shows nucleation of the amorphous phase even at 15 GPa,[6] the transition to the triclinic structure can be regarded as an intermediate stage of amorphization.[2]

In Refs. 21 and 22 it is assumed that an elastic instability at 25 GPa, at which the frequency of the soft acoustic modes becomes imaginary in the entire Brillouin zone, gives rise to amorphization of the α-quartz structure. In analyzing the microscopic origin of the softening of the phonon modes, these authors neglect the angle of twist. In our view this model is incomplete, and the authors themselves are of the opinion that it is hypothetical.[3] Other authors[1] assert that amorphization starts at a lower pressure, 21.5 GPa, because of dynamic instability, where the frequency of the soft mode becomes imaginary near the point (1/3, 1/3, 0) in the Brillouin zone. On this basis we believe that the completely symmetric τ_{A_1} and incompletely symmetric τ_{E_1} torsional oscillations make the main contribution to the elastic and dynamic instability, irrespective of which one plays the main role in the amorphization process and in the shear instability, which gives rise to the transition to the triclinic phase.

In conclusion, we have proposed a new valence-force model of the deformation of α-quartz, taking account of the distortions of the tetrahedra. According to this model the rotation angle of the tetrahedra at high pressures tends to saturation and therefore the effective stiffness of the structure with respect to this angle increases, which attests to an increase in the stability of the structure and cannot lead to instability. At the same time the smaller parameter — the angle of twist — starts to increase nonlinearly with pressure, and this results in softening of the low-frequency acoustic branch and leads to instability of the tetrahedra with respect to twisting, which gives rise to a transition to the triclinic phase and then to amorphization of the structure.

This work was supported by the Russian Fund for Fundamental Research (Grant No. 98-05-65658).

[1] G. W. Watson and S. C. Parker, Phys. Rev. B **52**, 13306 (1995).
[2] K. J. Kingma, R. J. Hemley, H. K. Mao, and D. R. Veblen, Phys. Rev. Lett. **70**, 3927 (1993).
[3] J. R. Chelikowsky, N. Troullier, J. L. Martins, and H. E. King Jr., Phys. Rev. B **44**, 489 (1991).
[4] J. S. Tse and D. D. Klug, Phys. Rev. Lett. **70**, 174 (1993).
[5] H. Grimm and B. Dorner, J. Phys. Chem. Solids **36**, 407 (1975).
[6] R. M. Hazen, L. W. Finger, R. J. Hemley, and H. K. Mao, Solid State Commun. **72**, 507 (1989).
[7] N. Binggeli and J. R. Chelikowsky, Nature (London) **353**, 344 (1991).
[8] J. S. Tse and D. D. Klug, Phys. Rev. Lett. **67**, 3559 (1991).
[9] K. J. Kingma, C. Meade, R. J. Hemley *et al.*, Science **259**, 666 (1993).
[10] G. Dolino and J. P. Bachheimer, Ferroelectrics **43**, 77 (1982).
[11] T. A. Aslanyan, A. P. Levanyuk, M. Vallade, and J. Lajzerowicz, J. Phys. C: Solid State Phys. **16**, 6705 (1983).
[12] M. Vallade, V. Dvorak, and J. Lajzerowicz, J. Phys. (France) **48**, 1171 (1987).
[13] D. Mukamel and M. B. Walker, Phys. Rev. Lett. **58**, 2559 (1987).
[14] J. Glinnemann, H. E. King, Jr., H. Schultz *et al.*, Z. Kristallogr. **198**, 177 (1992).
[15] M. B. Smirnov and A. P. Mirgorodsky, Phys. Rev. Lett. **78**, 2413 (1997).
[16] K. J. Kingma, H. K. Mao, and R. J. Hemley, High Press. Res. **14**, 363 (1996).
[17] A. N. Lazarev and A. P. Mirgorodsky, Phys. Chem. Miner. **18**, 231 (1991).
[18] A. G. Lyapin and V. V. Brazhkin, Phys. Rev. B **54**, 12036 (1996).
[19] J. S. Tse, D. D. Klug, Y. Le Page, and M. Bernasconi, Phys. Rev. B **56**, 10878 (1997).
[20] J. Badro, D. M. Teter, R. T. Downs *et al.*, Phys. Rev. B **56**, 5797 (1997).
[21] N. Binggeli, N. R. Keskar, and J. R. Chelikowsky, Phys. Rev. B **49**, 3075 (1994).
[22] J. R. Chelikowsky and N. Binggeli, Comput. Mater. Sci. **2**, 111 (1994).

Translated by M. E. Alferieff

Nanostructure and atomic ordering in vanadium carbide

A. A. Rempel'* and A. I. Gusev
Institute of Solid-State Chemistry, Urals Branch of the Russian Academy of Sciences, 620219 Ekaterinburg, Russia

(Submitted 10 February 1999)
Pis'ma Zh. Éksp. Teor. Fiz. **69**, No. 6, 436–442 (25 March 1999)

Nanostructured nonstoichiometric vanadium carbide $VC_{0.87}$ was obtained in powdered form using the ordering effect. The composition, structure, and properties of the carbide were studied by chemical and thermogravimetric analysis, gas chromatography, x-ray diffraction, optical and electronic microscopy, electron–positron annihilation, magnetic susceptibility, and microhardness methods. Nanostructured vanadium carbide $VC_{0.87}$ possesses the crystal structure of the cubic ordered phase V_8C_7 with space group $P4_332$. Vanadium carbide nanocrystallites are shaped in the form of 400–600 nm in diameter and 15–20 nm thick curved petals. The surface layer of the nanocrystallites contains defects of the vacancy agglomerate type. The microhardness of vanadium carbide, obtained by vacuum sintering of $VC_{0.87}$ nanopowder was 60–80 GPa, which is 3–4 times greater than the microhardness of coarse-grained vanadium carbide with the same composition and close to the hardness of diamond. © *1999 American Institute of Physics.* [S0021-3640(99)00906-8]

PACS numbers: 61.46.+w

The interest in nanocrystalline materials is due primarily to the expectation of various size effects on the properties of nanocrystallites and nanoparticles, whose size is comparable to or less than the characteristic correlation scale of the physical phenomenon or the characteristic length appearing in the description of any property or process.[1] However, thus far it has proved to be impossible to obtain many compounds in nanocrystalline state. Examples of such compounds are the strongly nonstoichiometric carbides MC_y ($0.5–0.7<y<1.0$) of group-IV and -V transition metals, which are second only to diamond and cubic boron nitride in hardness.

The carbides MC_y can contain from 0 to 50% structural vacancies in a nonmetallic sublattice.[2] The distribution of carbon atoms and structural vacancies over the sites of the nonmetallic sublattice can be disordered or ordered. The disordered carbides MC_y possess a cubic structure $B1$ and are thermodynamically stable at temperatures above 1400 K. At lower temperatures order–disorder phase transformations occur in nonstoichiometric carbides. These transformations lead to the formation of ordered phases with complicated superstructures.[2,3] Order–disorder transformations in carbides are first-order phase transitions[2,3] with an abrupt change in volume.[3,4] However, the ordering process is a diffusion process and therefore occurs not instantaneously but rather over several tens of

minutes. The synthesis temperatures of the carbides are 1400–1800 K. This is higher than the temperatures T_{trans} of order–disorder phase transformations. If cooling from the synthesis temperature to room temperature is performed rapidly, then there is not enough time for the ordering process to be completed and the nonstoichiometric carbide remains in a metastable disordered state. Since the lattice parameters of the disordered and ordered phases are different, stresses arise in the sample, and over time they can cause the crystallites to crack along the interfaces between the disordered and ordered phases. Nonstructural nonstoichiometric carbides can be obtained by regulating the sizes of the domains of the ordered phase.

In the present letter we report the results of a study of nanostructured nonstoichiometric vanadium carbide. This is the first nonstoichiometric carbide to be obtained in a nanocrystalline state. The ordering effect was used to produce the nanostructure. Ordering has not been previously used to form a nanostructure. Vanadium carbide as an object of investigation was chosen among all nonstoichiometric carbides because ordering is most strongly manifested in it.[4,5]

The initial disordered powdered vanadium carbide $VC_{0.87}$ with 1–2 μm particle sizes was obtained by carbothermal reduction of the oxide V_2O_5 followed by prolonged aging at 300 K in a closed vessel, which provided protection from the water vapor in air. The aged vanadium carbide powder was found to be very hygroscopic — immediately after being removed from the vessel the powder contained not more than 0.2 mass % of physically adsorbed water. After contact with air for several months the water content was 2.0 mass % and reached saturation. Ordinary coarse-grained vanadium carbide powder does not possess such hygroscopicity. Quantitative gas chromatography showed that besides water the aged $VC_{0.87}$ powder contains 3.1 ± 0.1 mass % chemisorbed oxygen. The negligibly small amount of oxygen (about 0.1 mass %) is dissolved in the vanadium carbide lattice and occupies sites in the nonmetallic lattice. A very small amount of the oxygen forms a surface oxide film with a thickness of 2–3 atomic monolayers. The film contains the oxide V_2O_3 and the homologous oxides V_nO_{2n-1}, which occupy positions between V_2O_3 and VO_3. To analyze the oxide film, vanadium carbide powder was heated in a dilute solution of HCl (concentration 0.36 mass %, pH = 1) at 330 K for several minutes. The presence of ions containing tri- and tetravalent vanadium in the powder can be judged according to the light-blue color of the solution. This confirms the presence of an oxide film on the surface of the vanadium carbide powder.

Chemical analysis showed that aged vanadium carbide powder possesses the composition $VC_{0.87}$ and corresponds to the upper limit of the region of homogeneity of the $B1$ cubic phase. The content of structural vacancies in the carbon sublattice is 13 at. %.

Under a microscope, using a magnification of approximately 100, the vanadium carbide powder consists of individual, irregularly shaped, 95–50 μm agglomerates consisting of approximately 1 μm particles. However, under higher magnifications it becomes clear that these particles have a complicated structure and in reality they consist of a collection of a large number of very small nanometer-size particles (in what follows we shall call them nanoparticles or nanocrystallites). Figure 1 shows a photomicrograph, obtained with a magnification of 10 000 in a DSM 982 Gemini high-resolution scanning electron microscope. It is clearly seen that each ~ 1 μm object resembles an opened rosebud or a very loose head of cabbage and consists of nanocrystallites. Under a magnification of 50 000 the nanocrystallites look like curved petals or sheets, which to a first

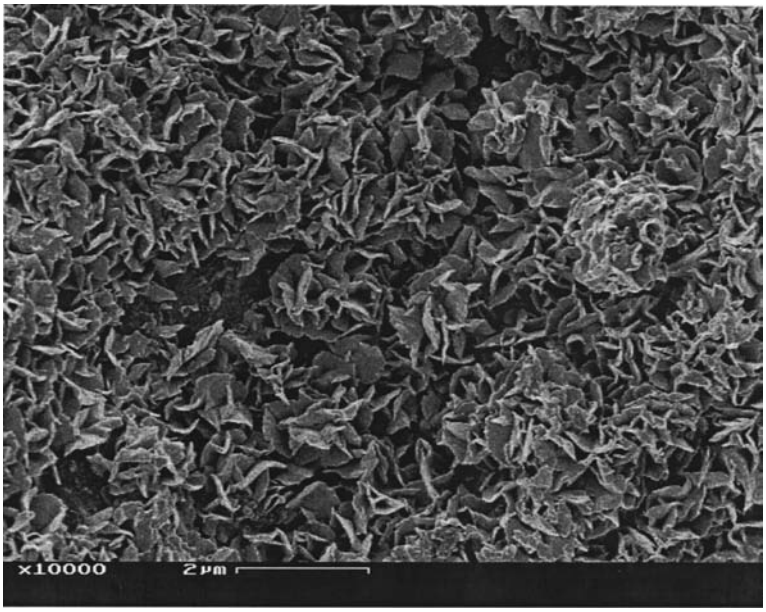

FIG. 1. Microstructure of vanadium carbide $VC_{0.87}$ powder subjected to prolonged aging at the temperature of and in an atmosphere of the surrounding medium (magnification 10 000).

approximation can be modeled by an approximately 15–20 nm thick disk ranging in diameter from 400 to 600 nm (Fig. 2). Even though from a volume standpoint such a disk corresponds to a quite large spherical particle 150–220 nm in diameter, because of the small thickness of the disk the ratio of its surface area S to the volume V is $S/V = 0.107–0.143\ \text{nm}^{-1}$, which corresponds to a specific surface area of the powder from 19 to 26 m^2/g. Electron microscopy also attests to a small size variance of the nanocrystallites in the powder.

Together with structural reflections, superstructural reflections corresponding to the cubic ordered phase V_8C_7 with space group $P4_332$ can be clearly seen in the x-ray diffraction pattern of vanadium carbide $VC_{0.87}$ (Fig. 3). The intensity ratio between the structural and superstructural reflections shows that the ordered phase occupies the entire volume of the material, i.e., the powder is a single-phase material. The lattice period of the ordered phase is 0.8337 ± 0.0001 nm. The lattice period of the ideal M_8C_7-type cubic superstructure (space group $P4_332$) is twice that of the disordered base phase $B1$.[2,3] Therefore for the vanadium carbide studied the period of the base phase is $a_{B1} = 0.41685$ nm. This is much greater (by 0.00047 nm) than the period of the disordered carbide $VC_{0.87}$. According to Ref. 5, such a large difference of the periods of the ordered and disordered carbides $VC_{0.87}$ can be observed only at or close to the maximum degree of ordering. The ratio of the intensities of the structural and superstructural reflections confirms that the degree of long-range order in vanadium carbide is close to the maximum value and that there is virtually no oxygen in the carbide lattice.

Analysis of the widths of the diffraction reflections did not show any deviations from the instrumental linewidth. The absence of broadening of the diffraction lines agrees

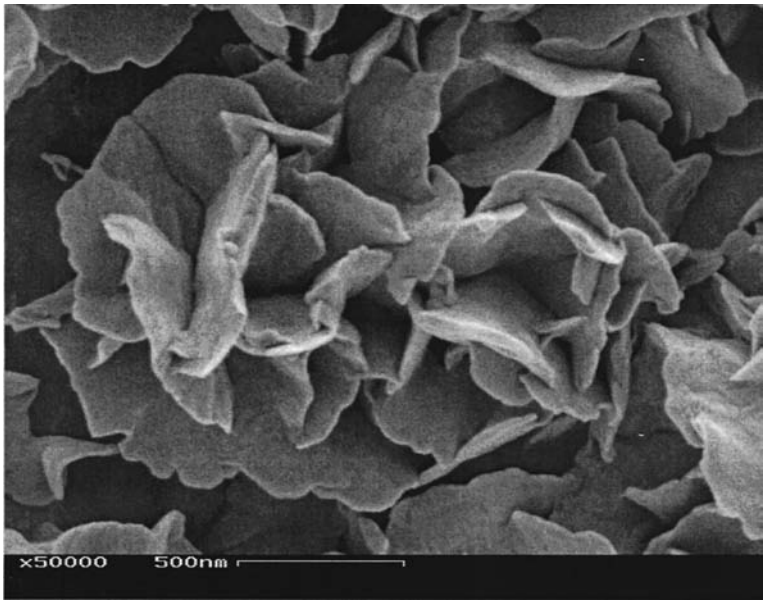

FIG. 2. Morphology of aged $VC_{0.87}$ powder particles under $\times 50\,000$ magnification — the approximately 1 μm particles consist of a collection of nanocrystallites in the shape of curved petals–disks ranging in diameter from 400 to 600 nm with a thickness of about 15–20 nm.

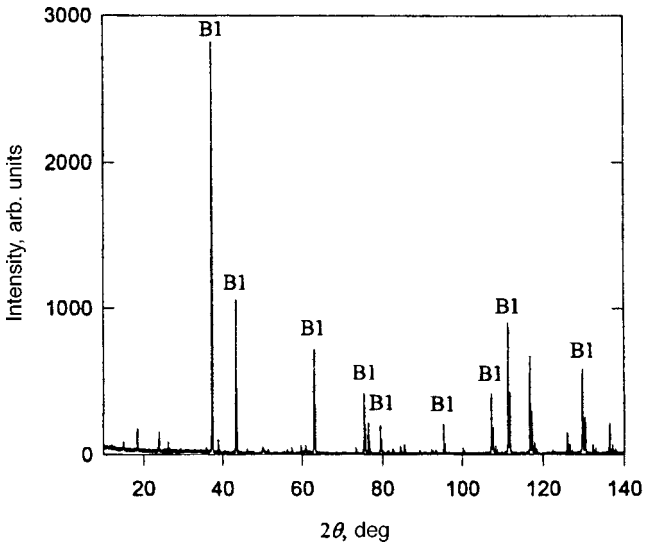

FIG. 3. X-ray diffraction pattern of $VC_{0.87}$ powder. The pattern contains structural reflections of the $B1$ phase (marked in the figure) and superstructural reflections corresponding to the cubic ordered structure V_8C_7 with space group $P4_332$ (Cu$K\alpha_{1,2}$ radiation was used).

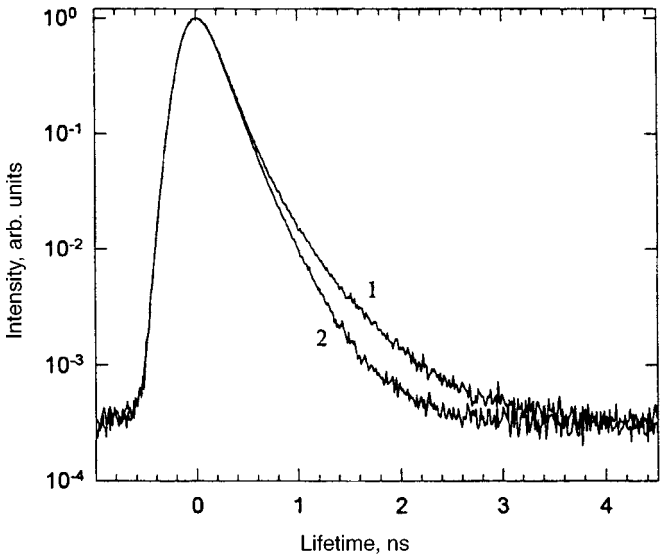

FIG. 4. Positron lifetime spectra of nanostructured vanadium carbide $VC_{0.87}$ powder (*1*) and a macrocrystalline vanadium carbide $VC_{0.87}$ (*2*).

with the quite large number of atoms in the nanocrystallites which scatter coherently.

The most effective and sensitive method for studying defects at interfaces and on the surfaces of nanoparticles is electron–positron annihilation. The capture of positrons by defects such as vacancies or nanopores results in a longer positron lifetime than in defect-free material.[6] The type of defect can be judged from the value of the lifetime.

The positron lifetime was measured in $VC_{0.87}$ carbide powder which was roasted beforehand at 400 K to remove water. For comparison, the positron lifetime in a sintered coarse-grained vanadium carbide sample with the same composition $VC_{0.87}$ was also measured. The spectra obtained (Fig. 4) are substantially different. The spectrum of the coarse-crystalline vanadium carbide sample contains only a short 157 ± 2 ps component, which corresponds to positron annihilation in a structural vacancy of the carbon sublattice.[7] Quantitative analysis of the spectrum of the powdered sample showed that it contains, together with the 157 ± 2 ps short component, a long 500 ps component with relative intensity $I_2=7\%$. According to Ref. 6, the long component is due to positron annihilation in large defects on the surfaces of the particles. Trapping of positrons by a structural vacancy signifies that positron diffusion over large distances does not occur; in this case, the component intensities are proportional to the volume fractions of the phases containing different types of defects. Thus the relative intensity I_2 of the long component corresponds to the surface volume fraction $\Delta V_s=\Delta D\cdot S/V$ in the vanadium carbide nanopowder. An estimate shows that the thickness of the surface layer is $\Delta D=0.5$–0.7 nm and corresponds to 3–4 atomic monolayers.

On the whole it follows from the positron lifetime data that the interior volume of the nanocrystallites contains only nonmetallic structural vacancies, while defects of the vacancy agglomerate type are present in the surface layer of the nanocrystallites.

The magnetic susceptibility method has been used previously to analyze the nanostructural state.[8] This method is sensitive to transformations occurring in nonstoichiometric carbides that are accompanied by changes in the electronic structure.[2,3,9] The magnetic susceptibility χ of nanostructured vanadium carbide $VC_{0.87}$ powder was measured in the temperature range from room temperature to 1200 K in a 1×10^{-3} Pa vacuum after treatment in hydrochloric acid to remove the surface film of vanadium oxides.

The susceptibility of vanadium carbide $VC_{0.87}$ at 300 K is 6×10^{-7} emu/g. The susceptibility increases very little with temperature, and the measured temperature dependence $\chi(T)$ is virtually identical to that[10] of coarse-grained carbide $VC_{0.87}$. This means that in the experimental temperature interval the nanostructure has virtually no effect on the electronic properties of vanadium carbide.

Nanostructured vanadium carbide $VC_{0.87}$ powder was cold-pressed at a pressure of 10 MPa. The compact density was 68% of the theoretical density of vanadium carbide. Sintering of the sample in a 1×10^{-3} Pa vacuum at temperatures ranging from 400 to 2000 K in steps of 100 K and holding at each temperature for 2 h did not greatly change the density, but it did make it possible to measure the Vickers microhardness. The measurements were performed under 200 and 500 g loads with a loading time of 10 s. No dependence of microhardness on the magnitude of the load was found to within the measurement accuracy. The microhardness H_V was 60–80 GPa, which is three to four times greater than the microhardness of macrocrystalline vanadium carbide (29 GPa under 0.1 and 0.2 kg loads),[11] and it is close to the microhardness of diamond. It is known that at 300 K the microhardness of nanomaterials is 2 to 7 times higher than H_V of ordinary polycrystalline material.[1] The much higher microhardness of the $VC_{0.87}$ carbide sample obtained from nanopowder can be explained by the Hall–Petch law, according to which H_V is proportional to $d^{-1/2}$ (d is the grain size). The analysis of the experimental data on the microhardness of compact nanocrystalline materials performed in Ref. 12 showed that the Hall–Petch law holds for grain size d ranging from 500 to 20 nm. The nanocrystallite sizes of the experimental carbide lie in this range.

The following model of the structure of nanocrystallites of vanadium carbide powder can be proposed on the basis of the experimental results. The nanocrystallites are strongly curved plates–disks, ranging in diameter from 400 to 600 nm and in thickness from 15 to 20 nm. The interior volume of a nanocrystallite consists of ordered carbide V_8C_7 with a high degree of long-range order and negligibly low dissolved oxygen content. Chemisorbed oxygen is present in the surface layer of the nanocrystallites in large quantities and a substantial number of vacancy agglomerates are present in the surface layer, attesting to its open structure. The thickness of the surface phase does not exceed 0.7 nm or four atomic layers.

The observed morphology of the nanocrystalline powder of nonstoichiometric vanadium carbide could be due to cracking of grains along the interfaces between the disordered and ordered phases. Indeed, high-temperature x-ray measurements[4] showed that at temperature 1413 ± 20 K an abrupt increase of the period of the crystalline fcc lattice by 0.0004 nm is observed as a result of an order–disorder phase transition $VC_{0.875}\rightarrow V_8C_7$; the domains of the ordered phase are $\sim$20 nm in size. According to Ref. 5, the ordering $VC_{0.875}\rightarrow V_8C_7$ occurs by a first order phase transition at temperature 1368 ± 12 K; at 300 K the parameter a_{B1} of the base crystalline lattice of the quenched disordered carbide $VC_{0.87}$ is 0.0002 nm smaller than in the ordered carbide with the same

oxygen content.[5] The difference in the volumes of the disordered and ordered phases results in the appearance of stresses and subsequent cracking along the interfaces between the phases. A different mechanism is also possible — cracking along domain walls of the ordered phase as a result of a misfit of the atomic structure of the antiphase domains and the appearance of stresses. To determine the mechanism leading to grain-size reduction on ordering, special investigations are required. Such a cracking effect due to prolonged aging and the appearance of stresses had been observed previously for a large ($\sim$25 mm long and $\sim$8–10 mm in diameter) single crystal of partially ordered nonstoichiometric niobium carbide $NbC_{0.83}$ with monoclinic (space group $C2/m$) structure of the type Nb_6C_5.

The nanostructure in vanadium carbide produces a factor of 3–4 increase in the microhardness. It can be assumed that order–disorder phase transitions which are accompanied by a volume change can be used to produce a nanostructured state in other materials, including strongly nonstoichiometric compounds.

We thank Mr. H. Labitzke for performing the electron microscopy of the vanadium carbide powder and O. V. Makarova and S. Z. Nazarova for assisting in the certification of the vanadium carbide. This work was supported by the Russian Fund for Fundamental Research (Projects Nos. 95-02-03549a, 98-03-32856a, and 99-03-32208a).

*e-mail: rempel@ihim.uran.ru; rempel@chem.ural.ru

[1] A. I. Gusev, Usp. Fiz. Nauk **168**, 55 (1998).
[2] A. I. Gusev and A. A. Rempel', *Structural Phase Transitions in Nonstoichiometric Compounds* [in Russian], Nauka, Moscow, 1988.
[3] A. A. Rempel', Usp. Fiz. Nauk **166**, 33 (1996).
[4] T. Athanassiadis, N. Lorenzelli, and C. H. de Novion, Ann. Chim. (Paris) **12**, 129 (1987).
[5] V. N. Lipatnikov, A. I. Gusev, P. Ettmayer, W. Lengauer, J. Phys.: Condens. Matter **11**, 163 (1999).
[6] R. Würschum and H.-E. Schaefer, in *Nanomaterials: Synthesis, Properties and Applications*, edited by A. S. Edelstein and R. C. Cammarata, Institute of Physics Publishing, Bristol, 1996, p. 277.
[7] A. A. Rempel, L. V. Zueva, V. N. Lipatnikov, and H.-E. Schaefer, Phys. Status Solidi A **169**, R9 (1998).
[8] A. A. Rempel, A. I. Gusev, R. R. Mulyukov, and N. M. Amirkhanov, Nanostruct. Mater. **7**, 667 (1996).
[9] A. I. Gusev and A. N. Zyryanova, JETP Lett. **69**, 324 (1999).
[10] R. Caudron, J. Castaing, and P. Costa, Solid State Commun. **8**, 621 (1970).
[11] L. Ramqvist, Jernkontors Annaler **152**, 467 (1968).
[12] A. I. Gusev, *Nanocrystalline Materials: Production Methods and Properties* [in Russian], Urals Branch of the Russian Academy of Sciences, Ekaterinburg, 1998.

Translated by M. E. Alferieff

Subsurface point and linear magnetic structural elements in weakly anisotropic magnets

V. E. Zubov, M. V. Gadzhilov, A. D. Kudakov,* and S. N. Kuz'menko
M. V. Lomonosov Moscow State University, 119899 Moscow, Russia

(Submitted 6 January 1999; resubmitted 17 February 1999)
Pis'ma Zh. Éksp. Teor. Fiz. **69**, No. 6, 443–446 (25 March 1999)

It is shown experimentally, using a magnetooptic micromagnetometer, that in single-crystal iron whiskers in an external magnetic field subsurface point magnetic elements with nonzero topological charge shift along linear elements, while elements with zero charge remain stationary. © *1999 American Institute of Physics.* [S0021-3640(99)01006-3]

PACS numbers: 75.60.Ch, 75.60.Ej, 75.50.−y

A wide spectrum of subsurface point and linear magnetic structural elements forms in weakly anisotropic magnets. The magnetization distribution in a 180-degree domain wall (DW) in an iron single crystal and the basic elements of the substructure of the wall in accordance with the results of Refs. 1 and 2 are displayed in Fig. 1a. The emergence of a DW at the surface is a linear magnetic structural formation of the horizontal Néel line (HNL) type. The experimentally observed structure corresponds to Hubert's model of an asymmetric Bloch wall.[3] In this model a transition occurs from the Bloch structure in the bulk of the crystal to a Néel structure in the the subsurface region via asymmetric bending of the DW (see Fig. 1a). The energy of such an HNL does not depend on the direction of bending of the DW at the surface. For this reason it can be divided into subdomains by several types of point elements: a subsurface Bloch point (SBP) and two types of emergence of vertical Bloch lines at the surface — VBL1 and VBL2 (see Fig. 1a). The experimental observation of a VBL2-type point singularity is a more complicated problem than the observation of SBP and VBL1, since only a small shift of the DW occurs at a transition through a VBL2 along the wall, while the Néel component of the magnetization does not change sign, in contrast to SBP and VBL1, at a transition through which the Néel component does change sign. It is shown below that these two groups of subsurface point singularities (SBP and VBL1, on the one hand, and VBL2 on the other) also differ substantially from one another from the standpoint of topology.

It can be concluded on the basis of the difference in the signs of the Néel component of the magnetization on different sides of the SBP and VBL1 that these structural elements should shift along the HNL in an external magnetic field directed parallel to the crystal surface and perpendicular to the DW (in the field H_x in Fig. 1a), while a VBL2 should not shift in a field H_x. The present work is devoted to checking these conclusions experimentally.

The topological characteristics of linear and point magnetic structural elements are presented below. The topological charge of a point magnetic element is determined by

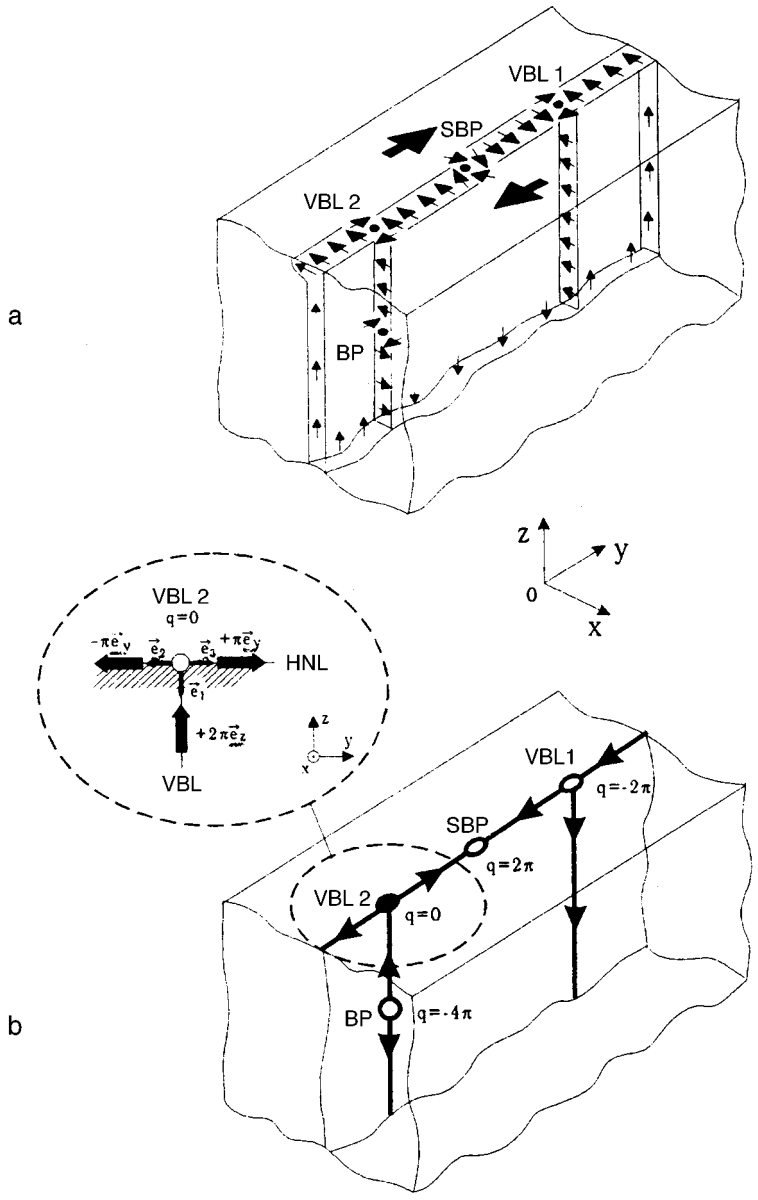

FIG. 1. a) Fragment of a 180-degree domain wall in iron, containing VBL, HNL, and point structural singularities — a volume BP, SBP, VBL1, and VBL2. b) Distribution of the fluxes of the gyrotropic vector in the micromagnetic structure displayed in Fig. 1a.

the expression $q=\int \mathbf{g}\cdot d\mathbf{S}$, where $\mathbf{g}=-\sin\theta(\nabla\theta\times\nabla\varphi)$ is the gyrotropic vector and θ and φ are angular coordinates of the magnetization vector in a spherical coordinate system. The integration extends over a closed surface enclosing the point element.[4,5] Since the magnetization vector field is continuous, the topological characteristics of point elements and

of the linear elements adjoining them should be matched with one another. The fact that a point element divides several linear elements (examples are VBL1 and VBL2) corresponds analytically to the separation of its topological charge far from the point singularity into several terms:

$$q = \oint\!\!\oint \mathbf{g}\cdot d\mathbf{S} = \sum_i \mathbf{e}_i \cdot \boldsymbol{\tau}_i . \tag{1}$$

Here $\mathbf{e}_i$ are unit vectors emanating from the point element (see inset in Fig. 1b), the vector $\boldsymbol{\tau}_i = \int_{S_i} \mathbf{g} dS$ is the flux of the gyrotropic vector associated with the linear element, and S_i are integration surfaces consisting of planes perpendicular to the vectors $\mathbf{e}_i$. The quantity τ is determined by the asymptotic behavior of the magnetization in a linear element:

$$\tau = (\cos\theta_1 - \cos\theta_2)(\varphi_2 - \varphi_1), \tag{2}$$

where θ_1, θ_2, φ_1, and φ_2 are the asymptotic values of the spherical coordinates of the magnetization vector in the direction of their variation.

For an HNL $\tau = \pm\pi$, and for a VBL $\tau = \pm 2\pi$. The topological charge of a point element can be calculated if τ_i in the linear elements emanating from it are known. Figure 1b shows the distribution of the fluxes of the gyrotropic vector $\boldsymbol{\tau}$ in the micromagnetic structure presented in Fig. 1a. For an SBP the topological charge is $\pm 2\pi$, while for a volume BP the topological charge is $\pm 4\pi$. The topological charge of a VBL1 can assume the values $\pm 2\pi$, i.e., VBL1 are topologically equivalent to SBP. The topological charge of VBL2 is zero.

Let us now consider the shift of the subsurface point magnetic structural elements in an external field. As samples we used single-crystal iron whiskers obtained by hydrogen reduction of iron halide salts. Samples with a square cross section with edge length $d = 30-150$ μm and length $L \sim 10$ mm with natural optically perfect (100) type faces were selected for the measurements. The samples contained one 180-degree DW (see Fig. 1a), located at the center along the axis of the crystal. A magnetic field H_x perpendicular to the plane of the DW was produced using Helmholtz coils and varied from -30 to $+30$ Oe. To suppress the coercivity of the point magnetic structural elements and the VBL, a ~ 40 kHz ac field H_y was used to excite oscillations of the DW with an amplitude of the order of the width of the wall. The shift of the magnetic structural elements in the constant field H_x and H_z becomes completely reversible (see Ref. 2 for a more detailed discussion). The investigations were performed using the magnetooptic micromagnetometer described in Ref. 1. The equatorial Kerr effect, due to the Néel component of the magnetization in the subsurface region of the DW, was measured. The method used to observe and determine the positions of the point singularities in the DW is described in detail in Ref. 1.

The results of the investigations in an iron single-crystal whisker with $d = 80$ μm are presented in Fig. 2. It is evident from the figure that the shift of the VBL1 (t) from its position of equilibrium in the absence of a field depends linearly on the field intensity H_x. The susceptibility of VBL1 was ~ 0.3 μm/Oe. The maximum shift of the VBL1 from the position of equilibrium in a field $H_x = \pm 30$ Oe was ± 9 μm. The position of VBL2 remains unchanged, to within the limits of accuracy of the measurements, for fields H_x in the range -30 Oe $\leqslant H_x \leqslant 30$ Oe (see Fig. 2). The possibility of SBP shifting

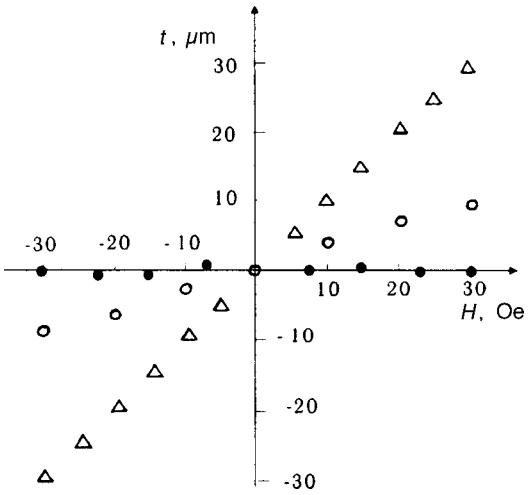

FIG. 2. Shift (t) of SBP, VBL1, and VBL2 in a constant field H_x from the position of equilibrium in an iron single-crystal whisker. Δ — SBP, ○ — VBL1, ● — VBL2.

in a field H_x was proved in Ref. 2. In the present work the susceptibility of SBP in a field H_x was measured in the same sample for comparison. The susceptibility of SBP was ~ 1 μm/Oe. The fact that the susceptibility of SBP is higher than that of VBL1 can be explained by the fact that in the bulk a VBL exerts a restraining force on VBL1 during motion in the field H_x, since the VBL does not shift under the action of this field.

This work was supported by the Russian Fund for Fundamental Research (Grant No. 97-03-32409a) and a Grant from the Ministry of Education of the Russian Federation.

*e-mail: kudakov@adk.phys.msu.su

[1] V. E. Zubov, G. S. Krinchik, and A. D. Kudakov, JETP Lett. **47**, 161 (1988).
[2] V. E. Zubov, G. S. Krinchik, and S. N. Kuz'menko, Zh. Éksp. Teor. Fiz. **99**, 551 (1991) [Sov. Phys. JETP **72**, 307 (1991)].
[3] A. Hubert, Z. Angew. Phys. **32**, 58 (1971).
[4] Malozemoff and J. C. Slonczewski, *Magnetic Domain Walls in Bubble Materials*, Academic Press, New York, 1979; Mir, Moscow, 1982.
[5] A. S. Shvarts, *Quantum Field Theory and Topology* [in Russian], Nauka, Moscow, 1989.

Translated by M. E. Alferieff

Optical conductivity in a simple model of a pseudogap state of a two-dimensional system

M. V. Sadovskiĭ*

Institute of Electrophysics, Urals Branch of the Russian Academy of Sciences, 620049 Ekaterinburg, Russia

(Submitted 17 February 1999)
Pis'ma Zh. Éksp. Teor. Fiz. **69**, No. 6, 447–452 (25 March 1999)

Calculations of the optical conductivity are performed in a simple model of the electronic spectrum of a two-dimensional system with ''hot regions'' on the Fermi surface. The model leads to a strong restructuring of the spectral density (pseudogap) in these regions. It is shown that this model makes it possible to reproduce qualitatively the basic features of the optical measurements in the pseudogap state of high-temperature superconducting cuprates. © *1999 American Institute of Physics.* [S0021-3640(99)01106-8]

PACS numbers: 74.25.Gz

Among the variety of anomalies of the normal state of high-temperature superconductors (HTSCs), of special interest is the observation of a pseudogap in their electronic spectrum at suboptimal current-carrier densities.[1,2] The most striking evidence in favor of this unusual state was obtained in angle-resolved photoemission spectroscopy experiments.[3,4] These experiments showed the existence of strongly anisotropic changes in the spectral density of the current carriers. Specifically, in these experiments the maximum width of the pseudogap was observed near the point $(\pi,0)$ in the Brillouin zone, while in the direction of the diagonal of the zone there was no pseudogap at all. Correspondingly, the Fermi surface breaks up near the point $(\pi,0)$, while near the diagonal it remains intact. In this sense it is said that the pseudogap possesses *d*-type symmetry, identical to the symmetry of the superconducting gap in these systems. These anomalies exist right up to temperatures $T \simeq T^*$, much higher than the superconducting transition temperature T_c.

A pseudogap also appears in the anomalies of the optical conductivity of an entire series of HTSC systems.[5–9] These anomalies reduce essentially to the existence of an anomalously narrow Drude peak (decrease of the scattering rate) at low frequencies and weak absorption through the pseudogap at higher frequencies.

A number of theoretical approaches attempting to explain the pseudogap anomalies exist. In the present letter we adopt an ideology based on the assumption that fluctuations of antiferromagnetic short-range order play the determining role (the ''hot spots'' model).[10,11] In this model it is possible to obtain an ''almost'' exact solution of the electronic spectrum problem, by summing the entire series of Feynman diagrams describing the interaction of the current carriers with antiferromagnetic fluctuations,[10–12] on the

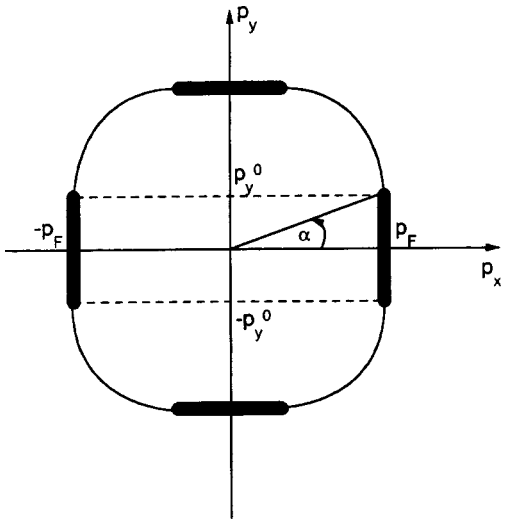

FIG. 1. The Fermi surface of a two-dimensional system. The thick lines, whose width is $\sim\xi^{-1}$, show the hot regions.

basis of a two-dimensional generalization of a one-dimensional model proposed earlier.[13–17]

Since serious computational difficulties, associated with the use of the ''realistic'' current-carrier spectrum, arise in the hot-spots model, here we shall use a greatly simplified model of the pseudogap state. This model was studied in Ref. 18 and is actually very close to the hot-spots model. Following Ref. 18, we assume that the Fermi surface of a two-dimensional electronic system has the form displayed in Fig. 1. A similar form of the Fermi surface was assumed in Ref. 19, where it was noted that this form is very close to that observed in Refs. 20 and 21 for a number of HTSC systems. We shall assume the short-range-order fluctuations to be static and Gaussian, and we determine their correlation function in the form[12,18]

$$S(\mathbf{q})=\frac{1}{\pi}\left\{\frac{\xi^{-1}}{(q_x-Q_x)^2+\xi^{-2}}\,\delta(q_y)+\frac{\xi^{-1}}{(q_y-Q_y)^2+\xi^{-2}}\,\delta(q_x)\right\}, \tag{1}$$

where $Q_x=Q_y=\pm 2p_F$. We shall assume that only electrons from the ''hot'' (flat) regions of the Fermi surface, which are shown in Fig. 1, interact with these fluctuations. We shall describe the effective interaction of these electrons with the fluctuations by the quantity $(2\pi)^2\Delta^2 S(\mathbf{q})$, where the parameter Δ, which has the dimensions of energy, determines the energy scale (width) of the pseudogap. Thus we assume that scattering by fluctuations is actually of a one-dimensional character. The choice of the scattering vector $\mathbf{Q}=(2p_F,2p_F)$ presumes incommensurate fluctuations. The commensurate scattering variant $\mathbf{Q}=(\pi/a,\pi/a)$ (where a is the lattice constant) can also be considered.

We assume that weak static scattering of arbitrary nature exists on the ''cold'' regions. I shall describe the rate of this scattering by the phenomenological parameter γ, assuming $\gamma\ll\Delta$ always, so that on the hot regions this scattering can be simply neglected. Correspondingly, the electronic spectrum on the cold regions is described by ordinary

expressions for the Green's functions in a system with weak scattering (Fermi liquid). In the limit $\xi\to\infty$ this model can be solved exactly by the methods proposed in Refs. 13 and 14, while for finite ξ it can be solved ''almost'' exactly (see Refs. 10–12) by the methods of Refs. 15–17.

We shall consider first the simplest case $\xi\to\infty$ where the effective interaction with fluctuations (1) acquires the simplest form

$$(2\pi)^2\Delta^2\{\delta(q_x\pm 2p_F)\,\delta(q_y)+\delta(q_y\pm 2p_F)\,\delta(q_x)\}. \tag{2}$$

In this case the entire perturbation series for both the single- and two-electron Green's function for an electron scattered by such fluctuations can be easily summed by the methods of Refs. 13 and 14. Specifically, in the case of incommensurate short-range order fluctuations the single-electron Green's function has the form

$$G(\epsilon,\mathbf{p})=\int_0^\infty d\zeta e^{-\zeta}\frac{\epsilon+\xi_{\mathbf{p}}}{\epsilon^2-\xi_{\mathbf{p}}^2-\zeta\Delta^2(\phi)}, \tag{3}$$

where $\xi_{\mathbf{p}}=v_F(|\mathbf{p}|-p_F)$ (v_F is the velocity on the Fermi surface), and $\Delta(\phi)$ for $0\leqslant\phi\leqslant\pi/2$ is given by

$$\Delta\phi\begin{cases}\Delta, & 0\leqslant\phi\leqslant\alpha,\quad \pi/2-\alpha\leqslant\phi\leqslant\pi/2\\ 0, & \alpha\leqslant\phi\leqslant\pi/2-\alpha\end{cases}, \tag{4}$$

where $\alpha=\tan^{-1}(p_y^0/p_F)$ and ϕ is the polar angle, determining the direction of the vector $\mathbf{p}$ in the (p_x,p_y) plane. For all other values of ϕ the quantity $\Delta(\phi)$ is determined in an obvious manner similarly to Eq. (4) from symmetry considerations. It is easy to see that by varying α in the range $0\leqslant\alpha\leqslant\pi/4$ we actually change the size of the hot regions on the Fermi surface where the nesting condition $\xi_{\mathbf{p}-\mathbf{Q}}=-\xi_{\mathbf{p}}$ holds. Specifically, $\alpha=\pi/4$ corresponds to a square Fermi surface on which the ''nesting'' holds everywhere. In what follows, all numerical results are presented for the quite arbitrarily chosen value $\alpha=\pi/6$. The qualitative dependences of a number of characteristics of the model on the parameter α are presented in Ref. 18. Outside the hot regions [second inequality in Eq. (4)] the Green's function (3) is simply identical to the Green's function of free electrons (actually, here it is also necessary to take account of only the weak scattering γ mentioned above).

The spectral density and density of states corresponding to the Green's function (3) are presented in Ref. 18 and demonstrate non-Fermi-liquid (pseudogap) behavior on the hot regions of the Fermi surface. The two-particle Green's function (the density–density response function) on the hot regions can be calculated by summing the corresponding diagrams completely, as done in the one-dimensional case in Refs. 13 and 14.

In this model the conductivity consists of additive contributions from the hot and cold regions. Specifically, for the real part we have

$$\mathrm{Re}\,\sigma(\omega)=\frac{4\alpha}{\pi}\,\mathrm{Re}\sigma_\Delta(\omega)+\left(1-\frac{4\alpha}{\pi}\right)\mathrm{Re}\,\sigma_D(\omega), \tag{5}$$

where, taking account of the results of Refs. 13 and 14,

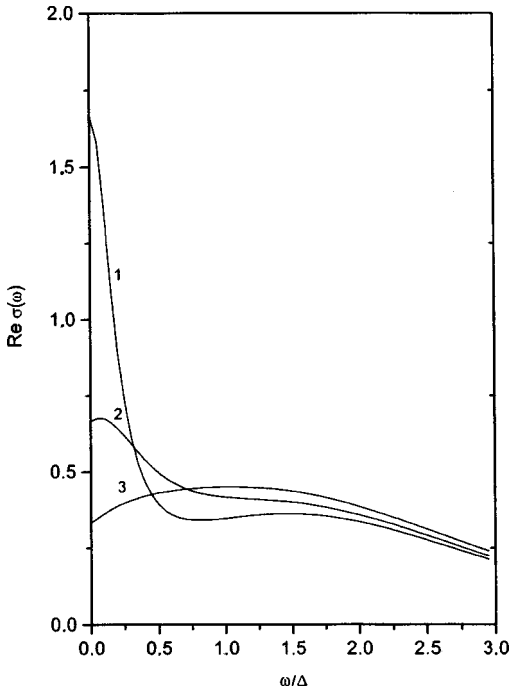

FIG. 2. Real part of the conductivity in a model with an infinite correlation length. The conductivity is given in units of $\omega_p^2/4\pi\Delta$. Curve *1* — $\gamma/\Delta=0.1$, *2* — $\gamma/\Delta=0.5$, *3* — $\gamma/\Delta=1.0$.

$$\mathrm{Re}\sigma_\Delta(\omega)=\frac{\omega_p^2}{4}\frac{\Delta}{\omega^2}\int_0^{\omega^2/4\Delta^2}d\zeta\,\exp(-\zeta)\frac{\zeta}{\sqrt{\omega^2/4\Delta^2-\zeta}}. \tag{6}$$

Here ω_p is the plasma frequency and

$$\mathrm{Re}\sigma_D(\omega)=\frac{\omega_p^2}{4\pi}\frac{\gamma}{\omega^2+\gamma^2} \tag{7}$$

is the ordinary Drude part of the conductivity from the cold regions.

Figure 2 shows the frequency dependence of the real part of the conductivity, calculated using Eqs. (5), (6), and (7) for various values of the parameter γ. Even in this very simple approximation this dependence closely resembles the experimental data obtained in Refs. 5–9. As the scattering rate γ increases on the cold regions, the characteristic Drude peak at low frequencies is suppressed.

The more realistic case of a finite correlation length of fluctuations of short-range ''antiferromagnetic'' order ξ in Eq. (1) can be analyzed by the methods of Refs. 15–17, which make it possible to find an ''almost exact''[12] solution of the problem. The following recurrence relation (representation in the form of a continued fraction[15]) arises for the one-electron Green's function on the hot regions:

$$G^{-1}(\epsilon,\xi_{\mathbf{p}})=G_0^{-1}(\epsilon,\xi_{\mathbf{p}})-\Sigma_1(\epsilon,\xi_{\mathbf{p}}), \tag{8}$$

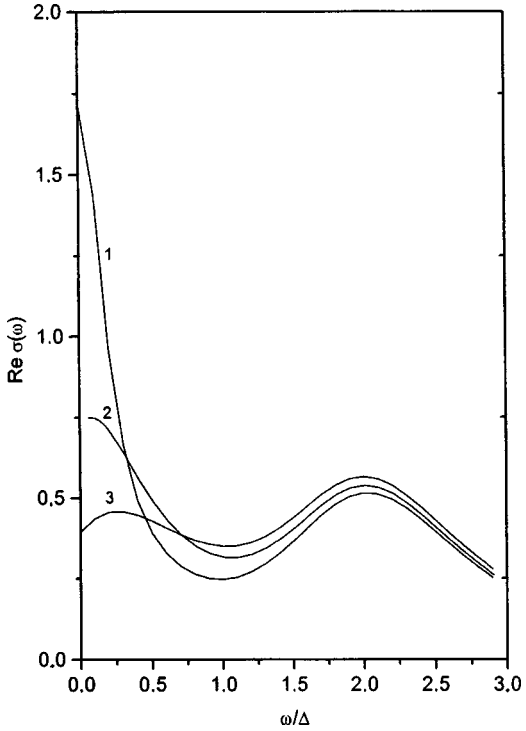

FIG. 3. Real part of the conductivity as a function of γ for fixed correlation length $v_F\kappa=0.5\Delta$. The conductivity is given in units of $\omega_p^2/4\pi\Delta$. Curve *1* — $\gamma/\Delta=0.1$, *2* — $\gamma/\Delta=0.5$, *3* — $\gamma/\Delta=1.0$.

where

$$\Sigma_k(\epsilon,\xi_{\mathbf{p}})=\Delta^2\frac{v(k)}{\epsilon-(-1)^k\xi_{\mathbf{p}}+ikv_F\kappa-\Sigma_{k+1}(\epsilon,\xi_{\mathbf{p}})}. \tag{9}$$

The combinatorial factor is

$$v(k)=\begin{cases}(k+1)/2 & \text{for odd } k,\\ k/2 & \text{for even } k\end{cases} \tag{10}$$

for the case of incommensurate short-range order fluctuations. In the commensurate case

$$v(k)=k. \tag{11}$$

In the spin-fermion model[10,11]

$$v(k)=\begin{cases}(k+2)/3 & \text{for odd } k,\\ k/3 & \text{for even } k.\end{cases} \tag{12}$$

For the vertex part, determining the density–density response function (two-particle Green's function) on the hot regions, we have the following recurrence relation (details can be found in Refs. 16 and 17 as well as in Ref. 11):

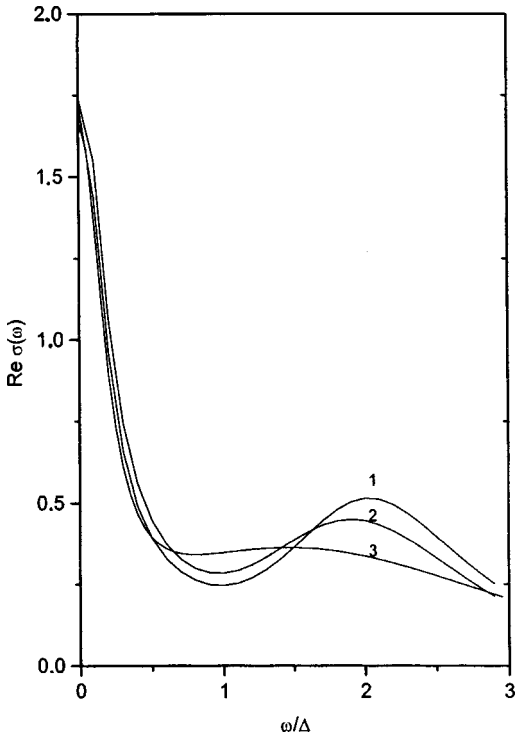

FIG. 4. Real part of the conductivity as a function of the correlation length for fixed $\gamma=0.2\Delta$. The conductivity is given in units of $\omega_p^2/4\pi\Delta$. Curve *1* — $v_F\kappa/\Delta=0.5$, *2* — $v_F\kappa/\Delta=1.0$, *3* — $v_F\kappa/\Delta=0$.

$$J^{RA}_{k-1}(\epsilon,\xi_{\mathbf{p}};\epsilon+\omega,\xi_{\mathbf{p+q}})$$
$$=e+\Delta^2 v(k)G^A_k(\epsilon,\xi_{\mathbf{p}})G^R_k(\epsilon+\omega,\xi_{\mathbf{p+q}})J^{RA}_k(\epsilon,\xi_{\mathbf{p}};\epsilon+\omega,\xi_{\mathbf{p+q}})$$
$$\times\left\{1+\frac{2iv_F\kappa k}{\omega-(-1)^k v_F q+v(k+1)\Delta^2[G^A_{k+1}(\epsilon,\xi_{\mathbf{p}})-G^R_{k+1}(\epsilon+\omega,\xi_{\mathbf{p+q}})]}\right\}, \qquad (13)$$

where e is the electron charge and the index $R(A)$ denotes the retarded (advanced) Green's function. The corresponding contribution of the hot regions to the conductivity $\mathrm{Re}\sigma_\Delta(\omega)$ in Eq. (5) can now be calculated just as in Refs. 16 and 17, while $\mathrm{Re}\sigma_\Delta(\omega)$ is once again determined by expression (7). The typical computational results are presented in Figs. 3 and 4 for the case of incommensurate fluctuations. Taking account of the combinatorics of the spin-fermion model gives negligible quantitative changes. The overall qualitative picture remains the same in the commensurate case. The conductivity is characterized by the presence of a quite narrow Drude peak at low frequencies $\omega<\gamma$, which originates from the cold regions on the Fermi surface, and a flat maximum at frequencies $\omega\sim 2\Delta$, which corresponds to absorption via a pseudogap that opens on the hot regions. The Drude peak rapidly broadens with increasing γ, and the presence of a maximum at low frequencies, which can be seen in Figs. 2 and 3, is due to traces of one-dimensional localization.[16,17] The dependence on the correlation length of the fluc-

tuations $\xi=\kappa^{-1}$ in the parameter range considered (the most interesting range) is quite weak. The qualitative picture obtained closely resembles the experimental data for a wide range of HTSC systems investigated in Refs. 5–9. Apparently, there is no difficulty in making a quantitative fit to the experimental data, using the known values $\omega_p \sim 1.5 - 2.5$ eV and $2\Delta \sim 0.1$ eV as well as the values of γ determined experimentally from the width of the Drude peak, by varying the free parameters α (size of the hot spots) and ξ (for which the well-known estimates from other experiments[11] can be used).

I thank É. Z. Kuchinskiĭ for helpful discussions.

This work was supported in part by Russian Fund for Fundamental Research Grant No. 99-02-16285 and as part of the Government Program ''Statistical Physics'' and Project No. 96-051 of the Government Program of the Russian Ministry of Science on High-Temperature Superconductivity.

*e-mail: sadovski@ief.uran.ru

[1] M. Randeria, Varenna Lectures, 1997; http://xxx.lanl.gov/abs/cond-mat/9710223.
[2] M. Randeria and J. C. Campuzano, Varenna Lectures 1997; http://xxx.lanl.gov/abs/cond-mat/9709107.
[3] H. Ding, T. Yokoda, J. C. Campuzano *et al.*, Nature (London) **382**, 51 (1996).
[4] H. Ding, M. R. Norman, T. Yokoya *et al.*, Phys. Rev. Lett. **78**, 2628 (1997).
[5] A. V. Puchkov, P. Fournier, D. N. Basov *et al.*, Phys. Rev. Lett. **77**, 3212 (1996).
[6] D. N. Basov, R. Liang, B. Dabrowski *et al.*, Phys. Rev. Lett. **77**, 4090 (1996).
[7] A. V. Puchkov, D. N. Basov, and T. Timusk, J. Phys.: Condens. Matter **8**, 10049 (1996).
[8] T. Startseva, T. Timusk, A. V. Puchkov *et al.*, http://xxx.lanl.gov/abs/cond-mat/9706145.
[9] T. Startseva, T. Timusk, A. V. Puchkov *et al.*, http://xxx.lanl.gov/abs/cond-mat/9812134.
[10] J. Schmalian, D. Pines, and B. Stojkovic, Phys. Rev. Lett. **80**, 3839 (1998).
[11] J. Schmalian, D. Pines, and B. Stojkovic, http://xxx.lanl.gov/abs/cond-mat/9804129.
[12] É. Z. Kuchinskiĭ and M. V. Sadovskiĭ, Zh. Éksp. Teor. Fiz. **115** (1999) [JETP (1995)], at press.
[13] M. V. Sadovskiĭ, Zh. Éksp. Teor. Fiz. **66**, 1720 (1974) [Sov. Phys. JETP **39**, 845 (1974)].
[14] M. V. Sadovskiĭ, Fiz. Tverd. Tela (Leningrad) **16**, 2504 (1974) [Sov. Phys. Solid State **26**, 1632 (1974)].
[15] M. V. Sadovskiĭ, Zh. Éksp. Teor. Fiz. **77**, 2070 (1979) [Sov. Phys. JETP **50**, 989 (1979)].
[16] M. V. Sadovskiĭ and A. A. Timofeev, Sverkhprovodimost: Fiz., Khim., Tekh. **4**, 11 (1991); Physica C **185–189**, 1431 (1991).
[17] M. V. Sadovskii and A. A. Timofeev, J. Mosc. Phys. Soc. **1**, 391 (1991).
[18] A. I. Posazhennikova and M. V. Sadovskiĭ, Zh. Éksp. Teor. Fiz. **115**, 632 (1999) [JETP **88**, 347 (1999)].
[19] A. T. Zheleznyak, V. M. Yakovenko, and I. E. Dzyaloshinskii, Phys. Rev. B **55**, 3200 (1997).
[20] D. S. Dessau, Z.-X. Shen, D. M. King *et al.*, Phys. Rev. Lett. **71**, 2781 (1993).
[21] Z. X. Shen and D. S. Dessau, Phys. Rep. **253**, 1 (1995).

Translated by M. E. Alferieff

Radiative emission of hot metallic clusters

B. M. Smirnov
Institute of High Temperatures, 127412 Moscow, Russia

H. Weidele
Laboratorium voor Vaste-Stoffysica en Magnetisme, B-3001 Leuven, Belgium

(Submitted 21 December 1998; resubmitted 8 February 1999)
Pis'ma Zh. Éksp. Teor. Fiz. **69**, No. 6, 453–458 (25 March 1999)

Analysis of experimental data on the relaxation of freely moving hot niobium and tungsten clusters shows that they are cooled as a result of radiative emission. The absorption cross sections per atom of niobium and tungsten clusters in the temperature range 3100–3700 K are $(4-7)\times 10^{-18}\,\mathrm{cm}^2$, and the absorption process loses its resonant character at these temperatures. © *1999 American Institute of Physics.* [S0021-3640(99)01206-2]

PACS numbers: 36.40.Mr

Radiative emission of hot metallic clusters governs the heat balance in clusters beams and plasmas. The radiation power can be expressed in terms of the absorption cross section of clusters, which may be a convenient parameter to characterize this process. A reliable method to measure the absorption cross section of clusters is photo-induced dissociation.[1] According to this concept, the absorption of photons leads to the decay of a cluster and, hence, to variation of its mass. The absorption cross section is obtained from measurement of the cluster mass abundance spectrum as a function of the laser intensity. This method has been used to measure the absorption cross sections for some cold metallic clusters (for example, Refs. 2–5). However, the radiative parameters of clusters in hot gases are expressed in terms of the absorption cross section of hot clusters, which may differ from those of cold clusters. These data may be derived from the measured relaxation parameters of hot clusters,[6–8] from which the cooling by radiation has been determined under experimental conditions. The goal of this paper is to find the absorption cross sections of hot clusters on the basis of their relaxation parameters.

The general principle of the experiments under consideration works as follows. Metallic clusters with a known range of sizes in a free cluster beam are heated by a laser pulse. Then a certain time after laser irradiation the radiative spectrum of the clusters is measured, and the signals are accumulated and summarized from many experimental cycles. As a result, we obtain the radiative spectrum of hot clusters as a function of the time delay after the excitation. Assuming a thermodynamic equilibrium within the radiating cluster, one can analyze from these data the character of cluster relaxation and radiation.

Heat balance of hot metallic clusters. For the relation between the absorption and emission rates of radiation for a cluster we use the Kirchhoff law. This corresponds to the

principle of detailed balance between the rates of direct absorption and the inverse process, and we obtain for the spectral power of cluster radiation[9]

$$p(\omega)=\hbar\omega i(\omega)\sigma_{\rm abs}(\omega), \tag{1}$$

where $\sigma_{\rm abs}(\omega)$ is the cluster absorption cross section and

$$i(\omega)=\frac{\omega^2}{\pi^2c^3}\left[\exp\left(\frac{\hbar\omega}{T}\right)-1\right]^{-1}. \tag{2}$$

Here $i(\omega)$ is the random photon flux of blackbody radiation inside a space where this radiation propagates (the temperature is expressed in energy units). From this we get for the spectral radiation power of a cluster

$$p(\omega)=\frac{\hbar\omega^3}{\pi^2c^3}\sigma_{\rm abs}(\omega)\left[\exp\left(\frac{\hbar\omega}{T}\right)-1\right]^{-1}. \tag{3}$$

Let us consider now the heat balance of a cluster which is heated by a laser pulse and is moving freely in vacuum. We make the assumption that the cluster is in thermodynamic equilibrium, which is supported by the kind of cooling processes observed. Then the state of the cluster is characterized by its temperature, and the heat balance equation during cooling has the form

$$C\frac{dT}{dt}=-\int\hbar\omega i(\omega)\sigma_{\rm abs}(\omega)d\omega-P_{el}-P_{\rm ev}, \tag{4}$$

where C is the cluster heat capacity; the first term on the right-hand side of this equation describes the cluster radiation, the second term takes thermionic emission of electrons into account, and the third term fragmentation. If one considers a bulk model for the cluster, then the heat capacity is expressed by the Dulong–Petit law $C=3n$, where n is the number of cluster atoms. This formula is valid at high cluster temperatures for $n\gg1$ when three classical vibrations per cluster atom are taken into account.

When analyzing the thermionic emission of electrons from the surface of a metallic cluster,[10] it is observed that the spectrum of the released electrons consists of two parts. The first part pertains to thermionic emission, and the second one has resonance character and is connected to the formation of autoionizing states. If the electron release proceeds under equilibrium conditions, the second mechanism gives only a small contribution to the total thermionic emission current which is then determined by the Richardson formula

$$i_{el}=A_RT^2W\exp(-W/T). \tag{5}$$

Here A_R is the Richardson–Dushman constant, which for niobium and tungsten has the values 57 and 75 $\rm A/cm^2K^2$ (Ref. 11), and W is the work function, which is equal to 4.0 and 4.5 eV, respectively.[12] We assume that the thermal energy of the released electrons $\sim T$ is small compared to the work function, and thus the cooling of the cluster as a result of the liberation of one electron is equal to the metal work function. Hence, the power of cluster cooling resulting from thermionic emission of electrons for a large metallic cluster is

$$P_{el}=4\pi r_W^2\cdot n^{2/3}i_{el}W=4\pi r_W^2\cdot n^{2/3}A_RT^2W\exp(-W/T), \tag{6}$$

TABLE I. Absorption parameters of niobium clusters derived from experiments[7,8] on the basis of formula (14).

ΔT, K	3479–3408	3408–3345	3345–3193	3550–3170
Δt, μs	3.7–5.9	5.9–8.0	8.0–18.7	6.4–31.1
$\sigma_{abs}(\omega_0)/n$, 0.01 Å^2	6.7	6.7	3.6	3.6
λ_0, μm	0.84	0.85	0.88	0.86

where r_W is the Wigner–Seitz radius, which is 1.68 Å and 1.60 Å for niobium and tungsten, respectively, and n is the number of cluster atoms. We assume the cluster to be large and spherical, so that the cluster radius can be estimated by $r=r_W n^{1/3}$. Thus formula (6) allows us to estimate the contribution of the thermionic emission for the cluster cooling process.

For this process it is of importance that the liberation of electrons leads to the charging of a cluster, which influences the subsequent release of electrons due to the attractive potential of the positively charged cluster. Indeed, the ionization potential of a large spherical cluster of radius r and charge Z is equal to

$$I_Z = W + Ze^2/r, \tag{7}$$

where the first term corresponds to the bulk metal work function W and the second term takes into account the electric Coulomb potential that the released electron must overcome to be removed from the cluster to infinity. Since the cluster is very large, we can neglect the Coulomb potential which results in a slightly increased estimate for the cooling power due to thermionic emission. If we solve equation (4), neglect radiation and fragmentation and use the Dulong–Petit formula for the cluster heat capacity, we get for the relaxation time

$$\tau_{el} = \tau_0 \exp(I_Z/T), \quad \tau_0 = \frac{3n^{1/3}e}{4\pi r_W^2 A_R I_Z^2}, \tag{8}$$

where e is the electron charge. We assume the cluster charge Z to be constant during this relaxation process.

Analyzing the character of the process under experimental conditions,[6–8] we find that $\tau_{el} \gg \tau_0$ by several orders of magnitude. For example, for niobium clusters in the size range of $n=13\,400$, whose parameters are given in Table I, $\tau_0 = 2.6\times 10^{-14}$ s, while typical relaxation times range from 10^{-6}–10^{-5} s. It follows from this that in the first stage of the relaxation process thermionic emission is of importance. Simultaneously with the cooling this leads to cluster charging. As a result, the cluster gets a positive charge, and after a certain time the thermionic emission process ceases. Note that the temperature decrease resulting from one thermionic emission event is relatively small. For example, in the above case the liberation of one electron from the niobium cluster decreases the cluster temperature by $\Delta T = 1.2$ K. Hence, in this cluster size range many electrons may be removed by thermionic emission before appreciable cooling occurs.

Let us determine the final cluster charge if the process proceeds at the temperature T. Then according to formula (8) the final cluster charge is $I_Z/T \approx 20$. We assumed here a weak dependence of τ_{el} on the type and parameters of the cluster. This gives for the final charge of a large metallic cluster

$$Z \approx \frac{r_W e^2 n^{1/3}}{e^2}(20T - W). \tag{9}$$

For example, in the above case for the niobium clusters of the size $n = 13\,400$ with an initial temperature of $T = 4000$ K this formula gives $Z = 8$. This corresponds to temperature difference of $\Delta T = 12$ K as a result of cooling by thermionic emission. Thus fast thermionic emission of the relaxing cluster leads in the first stage to cluster charging. On a longer time scale the cluster ceases to cool by thermionic emission, and the charged cluster cools by radiative emission.

In the next step let us evaluate the contribution due to cooling by the evaporation of atoms from the cluster surface rather than by thermionic emission. For a large cluster the power consumed by atom evaporation is equal to $P_{\text{ev}} = \varepsilon \nu_n$, where ε is the cluster binding energy per atom, which near the melting point is $\varepsilon = 7.35$ eV for bulk niobium and $\varepsilon = 8.6$ eV for bulk tungsten,[12] and ν_n is the evaporation rate of a large cluster with n atoms. Assuming that the cluster surface is comparable to the bulk surface, and furthermore is considered as a liquid droplet, we obtain for the evaporation rate[13]

$$\nu_n = k_0 n^{2/3} N_{\text{sat}}(T) \exp\left(-\frac{\varepsilon_n - \varepsilon_0}{T}\right), \quad k_0 = \pi r_W^2 \sqrt{\frac{8T}{\pi m}}\,. \tag{10}$$

Here m is the atomic mass, $N_{\text{sat}}(T) \propto \exp(-\varepsilon_0/T)$ is the number density of atoms at the saturated vapor pressure, and ε_n and ε_0 are the atom binding energies for the cluster and bulk system. Within the framework of the liquid drop model for the cluster we have $\varepsilon_n - \varepsilon_0 = \Delta\varepsilon/n^{1/3}$, and for large niobium and tungsten clusters we get $\Delta\varepsilon = 3.0$ eV, which can be derived from the surface tension of bulk metals.[12] The ratios of the evaporation power P_{ev} and the radiation power $P_{\text{rad}} = \int p(\omega)d\omega$ of tungsten clusters of the size $n = 200$ are $P_{\text{ev}}/P_{\text{rad}} = 0.09$ at $T = 3500$ K and $P_{\text{ev}}/P_{\text{rad}} = 0.003$ at $T = 3000$ K. Thus, the contribution of evaporation processes in the heat balance of relaxing clusters is small, but must be taken into account at high temperatures.

The small contributions of the thermionic emission and evaporation process to the cluster cooling can be explained as follows. The relaxation process proceeds at relatively low cluster temperatures, when the energy of one relaxation event ε is large compared to the thermal energy, so that the energy per event of the thermionic emission and evaporation process is larger than that of the radiative process. Since the rate of the relaxation processes, fragmentation and thermionic emission, is exponentially declining $\nu \sim \exp(-\varepsilon/T)$, the cooling of a freely moving cluster is mainly of a radiative character.

Finally, let us analyze the experimental data from the standpoint of a radiative character of cluster cooling. Note that the effective cluster temperature which is found from the measured radiative spectrum of the cluster coincides with the real cluster temperature only if the absorption cross section $\sigma_{\text{abs}}(\omega)$ does not depend on the wavelength. Below we assume a weak wavelength dependence for the absorption cross section, i.e., we take near a frequency ω_0

TABLE II. Absorption parameters of tungsten clusters derived from experiments[7] on the basis of formula (14).

ΔT, K	3605–3301	3301–3138	3500–3200	3500–3100	3700–3200
Δt, μs	8.3	9.5	16	17	18
$\sigma_{abs}(\omega_0)/n$, 0.01 Å^2	7.5	4.7	5.8	5.8	5.7
λ_0, μm	0.83	0.89	0.86	0.86	0.83

$$\sigma_{abs}(\omega)=\sigma_{abs}(\omega_0)+\frac{d\sigma_{abs}}{d\omega}(\omega-\omega_0). \tag{11}$$

The cluster heat balance in the course of relaxation is described by equation (4), where the radiative processes are described by

$$C\frac{dT}{dt}=-\int \hbar\omega i(\omega)\sigma_{abs}(\omega)d\omega. \tag{12}$$

Using formula (11) for the absorption cross section, we can rewrite this equation in the form

$$C\frac{dT}{dt}=-\frac{\sigma_{abs}(\omega_0)}{4}\kappa T^4, \tag{13}$$

where κ is the Stefan–Boltzmann constant. The optimal photon energy $\hbar\omega_0$ follows from the relation

$$\int_0^\infty(\omega-\omega_0)p(\omega)d\omega=0.$$

Restricting the exponential dependence in formula (2) by $i(\omega)\sim\omega^2\exp(-\hbar\omega/T)$ and taking into account that $\sigma_{abs}(\omega)\sim\omega$, we obtain for the optimal photon energy $\hbar\omega_0 \approx 5$ T. This relation is used in Tables I and II.

The solution of the heat balance equation (13) gives

$$\frac{\sigma_{abs}(\omega_0)}{n}=\frac{4}{\Delta t}\left(\frac{1}{T_2^3}-\frac{1}{T_1^3}\right). \tag{14}$$

Within the time interval Δt the cluster temperature changes from T_1 to T_2. Note that from general considerations (see, e.g., Ref. 14) one can derive that the absorption cross section of a particle, which is small compared to the radiation wavelength, is proportional to the particle volume or to the number of atoms which constitute the particle. Therefore, the relaxation time Δt from temperature T_1 to T_2 does not depend on the particle size.

Table I contains experimental data[7,8] for niobium clusters which are treated on the basis of formula (14). The same data for tungsten clusters with $n\approx 200$ (Ref. 6) are given in Table II. The average photoabsorption cross section per atom according to these data is $\sigma_{abs}(\omega_0)/n=(0.06\pm 0.01)$ Å^2. However, there is a large error in the treatment of the individual experimental curves, which exceeds the statistical error of all the data and the difference between niobium and tungsten clusters. The resulting photoabsorption cross

sections of hot niobium and tungsten clusters are more than an order of magnitude smaller than for cold lithium, potassium, and silver clusters.[2–5] This difference requires an additional analysis.

Considering the mechanism of the absorption process within the framework of two mechanisms,[15] one can understand the difference of the absorption cross sections for cold and hot clusters. In the first case absorption of cold clusters results from excitation of plasma oscillations, and the resonance width is due to electron scattering on nuclei. In the second case the absorption process is determined by atom resonance lines, the spectrum of which is split and broadened owing to interaction with surrounding atoms, and the resonance width is created also by scattering of individual electrons. An increase in temperature leads to a decrease of the typical time for electron scattering, which corresponds to broadening of the absorption spectrum and a decrease of the maximum absorption cross section. One can conclude on the basis of the experimental data for tungsten and niobium clusters that at temperatures above 3000 K the absorption process loses its resonance character and becomes like that of a blackbody.

This study was supported in part by RFFI (Grant #99-02-16094). H. W. is a Post-Doctoral Researcher of the European Community Training and Mobility of Researchers Program (TMR).

[1] M. L. Alexander, M. A. Johnson, N. E. Levinger, and W. C. Lindinger, Phys. Rev. Lett. **57**, 976 (1986).
[2] C. Bréchignac, Ph. Cahuzac, F. Carlier, and J. Leygnier, Chem. Phys. Lett. **164**, 433 (1989).
[3] C. Bréchignac, Ph. Cahuzac, N. Kebaili *et al.*, Phys. Rev. Lett. **68**, 3916 (1992).
[4] J. Tiggesbäumker, L. Keller, H. O. Lutz, and K.-H. Meiwes-Broer, Chem. Phys. Lett. **190**, 42 (1992).
[5] C. Bréchignac, Ph. Cahuzac, J. Leygnier, and A. Sarfati, Phys. Rev. Lett. **70**, 2036 (1993).
[6] U. Frenzel, A. Roggenkamp, and D. Kreisle, Chem. Phys. Lett. **240**, 109 (1995).
[7] U. Frenzel, U. Kalmbach, D. Kreisle, and E. Recknagel, Surf. Rev. Lett. **3**, 505 (1996).
[8] U. Frenzel, U. Hammer, H. Westje, and D. Kreisle, Z. Phys. D **40**, 108 (1997).
[9] B. M. Smirnov, Phys. Usp. **36**, 592 (1993); Int. J. Theor. Phys. **32**, 1453 (1993).
[10] H. Weidele, D. Kreisle, E. Recknagel *et al.*, Chem. Phys. Lett. **237**, 425 (1995).
[11] J. D. Cobine, *Gaseous Conductors*, Dover, New York, 1958.
[12] *Handbook of Chemistry and Physics*, 79th edition, edited by D. R. Lide, CRC Press, London, 1998-1999.
[13] B. M. Smirnov, Plasma Chem. Plasma Process. **13**, 673 (1993); Phys. Usp. **37**, 621 (1994).
[14] L. D. Landau and E. M. Lifshitz, *Electrodynamics of Continuous Media*, Addison-Wesley, Massachusets, 1960.
[15] B. M. Smirnov, Phys. Usp. **40**, 1117 (1997).